

Article

Molecular Mechanisms of Protein–Lipid Interactions and Protein Folding of Heterogeneous Amylin and Tau Oligomers on Lipid Nanodomains That Link to Alzheimer’s

Natalia Santos ¹, Luthary Segura ¹, Amber Lewis ¹, Thuong Pham ² and Kwan H. Cheng ^{1,2,*} 

¹ Neuroscience Department, Trinity University, San Antonio, TX 78212, USA; nsantos@trinity.edu (N.S.); lsegura1@trinity.edu (L.S.); alewis2@trinity.edu (A.L.)

² Physics Department, Trinity University, San Antonio, TX 78212, USA; tpham3@trinity.edu

* Correspondence: kcheng1@trinity.edu; Tel.: +1-210-999-8469

Abstract: The disruption of cell membranes by tau and amylin oligomers is linked to amyloid diseases such as Alzheimer’s and diabetes, respectively. The recent studies suggest that misfolded tau and amylin can form neurotoxic hetero-oligomers that are structurally different from homo-oligomers. However, the molecular interactions of these hetero-oligomers with the neuronal membranes remain unclear. Using MD simulations, we have investigated the binding behaviors, membrane disruption, and protein folding of hetero-oligomers on a raft membrane containing phase-separated lipid nanodomains like those found in neurons. We discovered that the hetero-oligomers bind to the liquid-order and liquid-disorder phase boundaries of the raft membrane. The major lipid-binding sites of these interactions include the L16 and I26 residues of amylin and the N-terminal of tau. Strong disruptions of the raft domain size by the hetero-tetramer were detected. Furthermore, the hetero-dimer disrupted the saturated phospholipid orientational order to a greater extent than the individual tau or amylin monomer. In addition, the constituent tau more strongly promoted the alpha-helix to the beta-sheet transition of the constituent amylin within the hetero-dimer when compared with the amylin monomer alone. Our results provide new molecular insights into understanding the neurotoxicity of the hetero-oligomers associated with the cross-talk between amyloid diseases.

Keywords: amyloid aggregates; protein folding; molecular dynamics; lipid rafts; protein misfolding disease; Alzheimer’s; diabetes



Citation: Santos, N.; Segura, L.; Lewis, A.; Pham, T.; Cheng, K.H. Molecular Mechanisms of Protein–Lipid Interactions and Protein Folding of Heterogeneous Amylin and Tau Oligomers on Lipid Nanodomains That Link to Alzheimer’s. *Macromol* **2023**, *3*, 805–827. <https://doi.org/10.3390/macromol3040046>

Academic Editor: Alejandro Baeza

Received: 12 October 2023

Revised: 4 December 2023

Accepted: 13 December 2023

Published: 15 December 2023



Copyright: © 2023 by the authors. Licensee MDPI, Basel, Switzerland. This article is an open access article distributed under the terms and conditions of the Creative Commons Attribution (CC BY) license (<https://creativecommons.org/licenses/by/4.0/>).

1. Introduction

The misfolding and subsequent aggregation of amyloidogenic proteins, e.g., amylin and tau, have been associated with the progression of amyloid diseases, e.g., type 2 diabetes (T2D) and Alzheimer’s (AZ), respectively. The major cellular targets of these misfolded amylin and tau aggregates are the beta cells in the pancreas [1] and neurons in the brain [2], respectively. However, recent in vivo and clinical studies have provided strong evidence that the cross-seeding of misfolding amylin and tau aggregates can occur in the brain [3,4]. This cross-seeding process results in the formation of heterogeneous amyloid aggregates that are more neurotoxic than the tau aggregates alone [3,5,6]. Additionally, a recent in vitro study [7] has indicated that the hetero-complexes of amylin and tau in solution can be formed with low concentrations of peptides. Furthermore, the protein secondary structures of these hetero-complexes are very different from those of the homo-complexes [7]. At present, the detailed molecular structures of these heterogeneous amylin–tau aggregates in a solution and on the targeted neuronal membranes are still unknown.

Clinically, the presence of microscopic, water-insoluble, beta-sheet-rich fibrils of amylin and tau have been established as major histopathological markers in T2D [8] and AZ [2], respectively. However, the recent in vitro cellular and lipid membrane investigations [9–11] have concluded that the nanoscopic and highly disordered amylin or tau

oligomers are more neurotoxic than the mature amylin or tau fibrils. In addition, the early molecular events of protein–lipid interactions and the subsequent surface-induced protein folding of these disordered oligomers upon their binding to the beta cell membranes in the pancreas or the neuronal membranes in the brain may play a critical role in the pathogenesis of T2D or AZ, respectively. However, the details of these molecular events for heterogeneous amylin–tau oligomers interacting with neuronal membranes that link to the prevalent cross-talking between AZ and T2D remain unclear. Also, the direct comparison of these amylin–tau hetero-oligomers with homo-oligomers consisting of individual amylin or tau and their effects on membrane structure disruptions, or membrane damage, has not been conducted. Furthermore, the protein’s secondary structures, particularly the alpha-helix and beta-sheet conformations, of the constituent amylin or tau protein within the hetero-oligomer when compared with those of the same protein in the homo-oligomer have not been explored. To address these issues, this computational study aims at investigating the lipid binding behaviors, membrane damage, and protein-folding of both the hetero-oligomers and homogeneous-oligomers of different sizes.

In this work, we have created hetero-oligomers in a solution based on the known atomistic (AA) Cryo-EM structures of the full-length, 37-residue-long amylin [12] and a 130-residue-long truncated human tau peptide containing four microtubule binding repeats [13]. We have used a self-aggregation process based on coarse-grained (CG) molecular dynamics (MD) simulations [14,15] to create these hetero-oligomers. Here, the membrane binding events of these hetero-oligomers to phase-separated lipid nanodomains that mimic the raft membrane domains were investigated. Our model raft membrane contains saturated phosphatidylcholine (PC), unsaturated PC, and cholesterol. Under physiological conditions, highly dynamic and phase-separated liquid-ordered (Lo), liquid-disordered (Ld), and mixed Lo/Ld (Lod) domains are spontaneously formed on the microsecond time scale. The interactions of the hetero-oligomers with these lipid domains were examined via up to 10 μ s of CG simulations. Important protein–lipid interaction events, such as the binding kinetics, lipid domain preference, residue-resolved binding patterns, and domain disruptions, were systematically investigated. To investigate the local membrane disruptions and protein folding, we have used a CG-to-AA resolution [16] transformation followed by 100 ns-long AA simulations to examine the lipid orientational order and protein-folding events of the membrane-bound hetero-oligomers with atomistic details.

Our combined multiscale, CG and AA, MD simulation approach, therefore, has allowed us to sample sufficient translational and rotational conformational phase space of the complex protein–lipid binding events on a physiologically relevant microsecond scale and explore the details of protein-induced membrane damage and protein folding with atomistic details. We have discovered that the hetero-oligomers bind specifically to the Lod domain, with the hydrophobic L16 and I26 residues of the amylin and the *N*-terminal of tau as the major lipid binding sites. Strong disruptions of the lipid domain size and localized lipid orientational orders by the hetero-oligomers were detected. Our results provide new insights into understanding the unknown molecular mechanisms of protein-induced membrane damage and surface-induced protein folding on neuronal membranes associated with the cross-seeding of amylin and tau aggregates in the brain. These molecular mechanisms provide new knowledge of the cross-talk between T2D and AZ. In addition, the simulated atomistic structures of hetero-oligomers are useful for future therapeutic interventions such as virtual drug discovery, targeting the membrane-attack complexes associated with the co-localized amylin and tau oligomers in the brain.

2. Materials and Methods

2.1. Modeling Heterogeneous Tau–Amylin Oligomers

Our heterogeneous tau–amylin oligomers, or hetero-oligomers, were generated from two independently equilibrated tau and amylin monomers, as shown in Figure 1. The structures of these monomers were obtained from our recent studies on homogeneous tau [14] and amylin [15] oligomers, respectively. In brief, each tau or amylin monomeric

structure was created by first extracting a peptide chain from a truncated, atomistic (AA) Cryo-EM pentamer structure [12,13], as shown in Figure S1. After attaching a random coil segment to the *N*-terminal of the extracted chain followed by energy minimization, the AA 37-residue-long amylin and 130-residue-long tau peptides were separately simulated [17]. Using an AA-to-coarse grained, or AA-to-CG resolution transformation procedure, a CG monomer of either amylin or tau peptide was subsequently created [18].

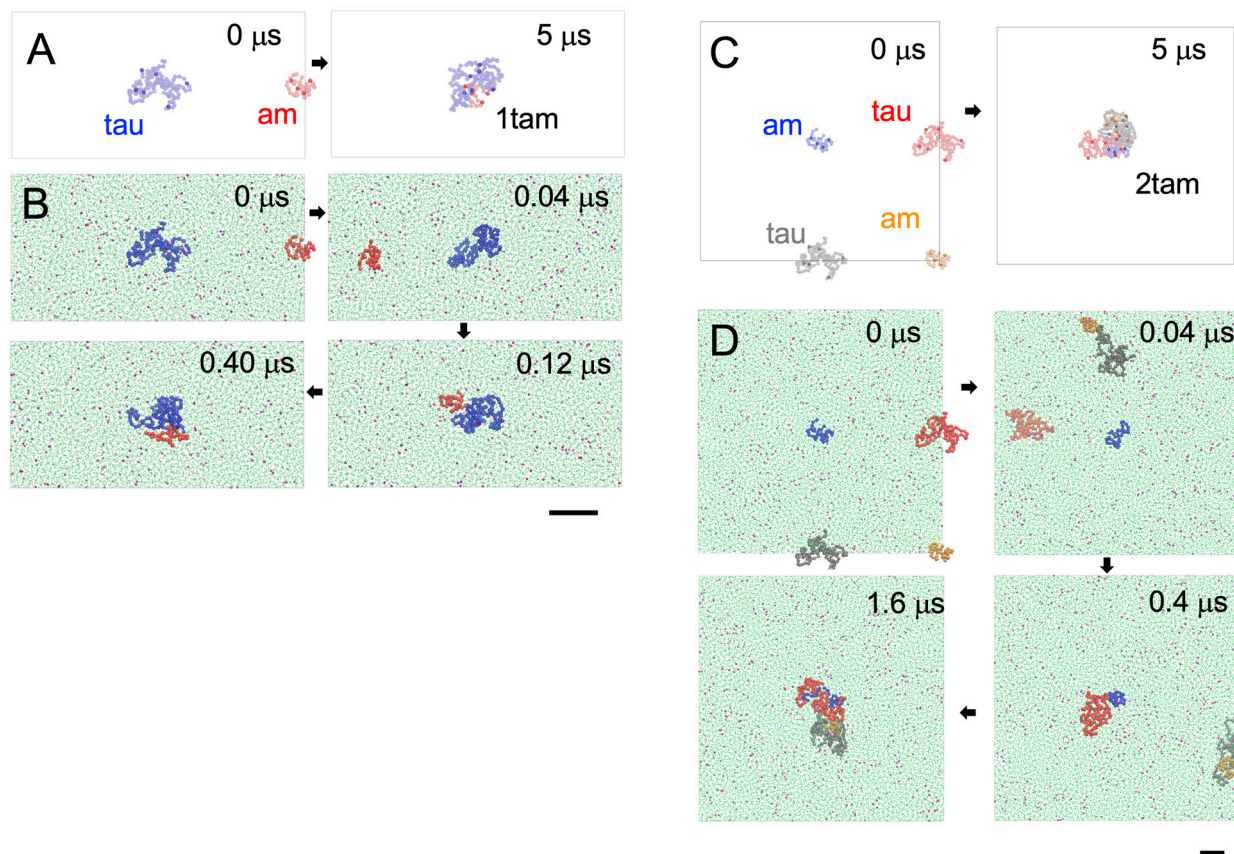


Figure 1. Modeling heterogeneous tau–amylin oligomers in solution. The initial (0 μ s) and final (5 μ s) CG structures of 1tam (A) and 2tam (C) in solution and their formation evolutions (B,D) from tau and am monomers are given. Water and ion CG atoms are as green dots and purple beads, respectively. The protein structures are shown in a backbone ribbon form with chain A in blue, chain B in red, chain C in gray, and chain D in orange. All CG simulations were performed in 0.1 M NaCl and under physiological conditions of 1 atmosphere and 310 K. A scale bar of 2 nm is shown.

The above monomer of amylin or tau was solvated in 0.1 M NaCl and underwent an energy minimization with position restraints to reduce the local high-energy-level structures between the solvent and protein atoms [19]. This energy-minimized structure in solution underwent a 5 μ s-long CG MD simulation in the NPT ensemble under the physiological conditions at 1 atmospheric pressure and 310 K using the Martini-2.20 CG force field [18], and it was ran on the GROMACS-4.67 MD simulation program [19]. At the end of the CG MD simulation, the equilibrated monomer structures of tau and amylin were finally obtained independently.

The hydrophobicity profiles of amylin and tau monomers in the form of hydrophathy index vs. protein residue plots are shown in Figure S1B,G, respectively [20,21]. Using a 5-point moving average fit to the hydrophathy index plots, the major hydrophobic residues of amylin at C7, L16, I26, and V32, and those of tau at V6, I35, I66, I86, I112, and V21, respectively, were determined from the peaks in the hydrophathy plots (Figure S1). The

details of identifying the hydrophobic residues of amylin and tau peptides have been described elsewhere [14,15].

The hetero-dimer was simulated in a rectangular simulation box of size $\sim 21 \times 11 \times 11 \text{ nm}^3$, as shown in Figure 1A. First, the equilibrated tau and amylin monomers were placed at the origin $(0, 0, 0)$ and $(L_x/2, 0, 0)$ locations, respectively, of the simulation box, where L_x is the width of the box along the x -direction. The hetero-tetramer was simulated in a larger rectangular box of size $\sim 21 \times 21 \times 11 \text{ nm}^3$. The first amylin monomer was placed at the origin $(0, 0, 0)$. Afterward, two tau monomers were placed at $(L_x/2, 0, 0)$ and $(0, -L_y/2, 0)$, and the second amylin monomer was placed at $(L_x/2, -L_y/2, 0)$. Here, L_x and L_y are the widths of the simulation box along the x - and y -directions, respectively.

With the above symmetric placements of hetero-monomers, the initial separation between the tau monomer and the amylin monomer was $\sim 10 \text{ nm}$ in both the dimeric and tetrameric simulation designs. In contrast, the initial separation between all the homogeneous monomers was $\sim 14 \text{ nm}$ in the tetrameric simulation design. Each of the above simulation boxes containing the amylin and tau monomers was then solvated in 0.1 M NaCl . After an identical energy minimization with position restraints followed by a $5 \mu\text{s}$ -long CG MD simulation [18] procedure as described above, the hetero-dimer or -tetramer, or 1tam or 2tam, were created via the self-aggregation procedure.

During the CG simulations, we observed that these separated tau and amylin monomers quickly established contact and formed a highly dynamic hetero-dimeric (1tam) or hetero-tetrameric (2tam) at 0.12 or $1.6 \mu\text{s}$, respectively. We noticed that the individual tau and amylin chains inside the 1tam or 2tam complex remained attached throughout the entire $5 \mu\text{s}$ -long simulation after establishing firm contact at those time points, as shown in Figure 1. Videos S1 and S2 in the Supplementary Materials demonstrate these self-aggregation events of 1tam and 2tam in the solution.

The locations of the major hydrophobic residues (see above) of amylin and tau in the homo-oligomers (Figure S1) and hetero-oligomers (Figure 1) were highlighted before and after the self-aggregation of the oligomers. We noticed that these hydrophobic residues remain randomly distributed before and after the $5 \mu\text{s}$ -long CG simulations for the hetero-oligomers (Figure 1) and the homo-oligomers (Figure S1). Upon equilibration, these $5 \mu\text{s}$ -1tam and -2tam structures were used as the starting protein structures for exploring the protein binding events of the hetero-oligomer to the raft membrane, as described below.

Note that a similar self-aggregation procedure was employed to generate the homo-amylin dimer (2am) and tetramer (4am), as well as the homo-tau dimer (2tau), and tetramer (4tau) from the equilibrated tau monomer (1tau) and amylin monomer (1am). The detailed steps of simulating these homo-tau and -amylin oligomers have been given elsewhere [14,15].

2.2. Modeling of the Raft Membrane

Our raft membrane is a self-assembled lipid bilayer containing saturated and unsaturated phosphatidylcholine (PC) and cholesterol (CHOL) in water with a size of $\sim 21 \times 21 \times 20 \text{ nm}^3$. Briefly, our simulated raft membrane has 828 saturated dipalmitoyl (or $2 \times \text{C16:0}$)-PC (DPPC), 540 unsaturated dilinoleoyl (or $2 \times \text{C18:2}$)-PC (DLPC), 576 CHOL, and 66,741 water molecules. Here, both the *sn*-1 and *sn*-2 acyl chains of DPPC are fully saturated, while those of DLPC are unsaturated and contain two double bonds in each acyl chain. Under the physiological conditions of 0.1 M NaCl , 1 atmospheric pressure, and 310 K , our simulated raft membrane contains highly dynamic, ordered DPPC-rich and CHOL-rich (Lo), disordered DLPC-rich (Ld), and mixed DPPC-DLPC (Lod) domains for up to $20 \mu\text{s}$ of CG simulations. Our simulated Lo, Ld, and Lod domains are structurally similar to the lipid raft, the non-raft, and the boundary between the raft and non-raft regions, respectively, found in the plasma membranes of most mammalian cells, including neurons [22–25]. The details of the construction of the raft membrane can be found elsewhere [26,27].

2.3. Simulations of Heterogeneous Oligomer Binding to the Raft Membrane

To simulate protein binding to the raft membrane, each equilibrated hetero-oligomer, 1tam or 2tam, was placed at a distance above the raft membrane surface without being in contact with the lipids of the membrane, as demonstrated in Figure 1. To improve the phase sampling of protein–membrane binding events, three independent simulation replicates were created for each oligomer–raft starting complex: replicate 1, replicate 2, and replicate 3. Here, replicate 1 represents placing the protein above the center of the surface of the lipid leaflet (upper leaflet), with the minimum distance between any atom of the protein and any atom of the lipid > 5 nm. Replicates 2 and 3 were subsequently created with the protein position shifted +2 nm and −2 nm along the *x*-direction relative to the protein position of replicate 1, respectively. Upon generating the initial structure of each replicate, the same CG MD simulation procedure as that used for preparing the oligomer or raft membrane in a solution was performed for 10 μs or longer.

Using the MD simulation visualization program VMD [28], the time-resolved protein binding event of each replicate was carefully examined. For 1tam, stable membrane binding events were observed at the time intervals from 0.2 to 10 μs, 2 to 10 μs, and 3 to 10 μs for replicates 1, 2, and 3, respectively. For the 2tam, replicate 1 did not bind to the membrane within 15 μs of simulation, replicate 2 exhibited two independent membrane binding events from 1.1 to 4.8 μs and 11.2 to 15 μs, and replicate 3 showed a single membrane binding event from 4 to 10 μs. Therefore, we have successfully obtained three independent membrane binding events for either 1tam or 2tam from multiple replicates using the CG simulations.

Figure 2A,B demonstrates the structures of the replicate 3 of the 1tam/raft complex and that of the 2tam/raft complex, respectively, at 0 and 10 μs. In the absence of the oligomer binding at 0 μs, the raft membrane exhibited phase-separated lipid domains in both the transverse and lateral views. These lipid domains are DPPC- and CHOL-enriched Lo shown in green, DLPC-enriched Ld shown in orange, and interfacial or mixed DPPC/DLPC Lod (boundaries between the green and orange patches). Each oligomer bound to the boundary region or Lod domain as shown in the 10 μs structures, as given in Figure 2A,B. Videos S3 and S4 in the Supplementary Materials demonstrate the transverse and lateral views of the protein/raft binding events as well as the dynamic nature of the lipid domains of the 1tam/raft complex.

After the CG simulation, the stable CG oligomer/raft complex from each replicate containing the membrane-bound oligomer was converted to an AA structure by a CG-to-AA resolution transformation procedure [16]. The transformed AA structure was equilibrated with similar energy minimization and position-restraining procedures as in the simulations of the CG oligomer–raft complexes. However, instead of the Martini CG force fields, the atomistic AMBER99SB [29] for proteins and SLIPIDS for lipids force fields [30,31] were used in all the AA MD simulations up to 100 ns. The final 100 ns AA structures of the representative replicates of the 1tam/raft and 2tam/raft complexes are illustrated in Figure 2C,D, respectively.

2.4. Classifications of Lipid Domains and Annular Lipids

The phase-separated lipid domains, Lo, Ld, and Lod, of our raft membrane, as described above, were classified using a data clustering tool, *g_select*, from GROMACS 4.6.7 [19]. This clustering tool was based on a proximity threshold of 0.5 nm between any atoms of DPPC and DLPC, as described in detail elsewhere [26]. Briefly, in the presence or absence (control) of membrane-bound oligomers, all the PC molecules in the raft membrane were classified into Lo-DPPC, Ld-DPPC, and Lod-PC. Here, the Lo-DPPC group consists of DPPC in the Lo domain, the Ld-DLPC group consists of DLPC in the Ld domain, and the Lod-PC group contains both DPPC and DLPC in the boundary Lod domain. Similarly, all the CHOL molecules were classified into the Lo-CHOL, Ld-CHOL, and Lod-CHOL groups, for which at least one CHOL atom is within 0.5 nm of the PC lipid atoms in the Lo, Ld, and Lod domains, respectively. Therefore, the Lo-DPPC and Lo-CHOL groups consist of lipid molecules residing in the highly ordered Lo domains. The Ld-DLPC and Ld-CHOL groups

represent the lipid molecules made up of the highly disordered Ld domains. Finally, the Lod-PC and Lod-CHOL represent the lipid molecules in the boundary region between the Lo and Ld domains. Detailed description of classifying lipid domains in the presence or absence of membrane-bound protein can be found elsewhere [26].

Tau-amylin oligomers binding to the raft membrane

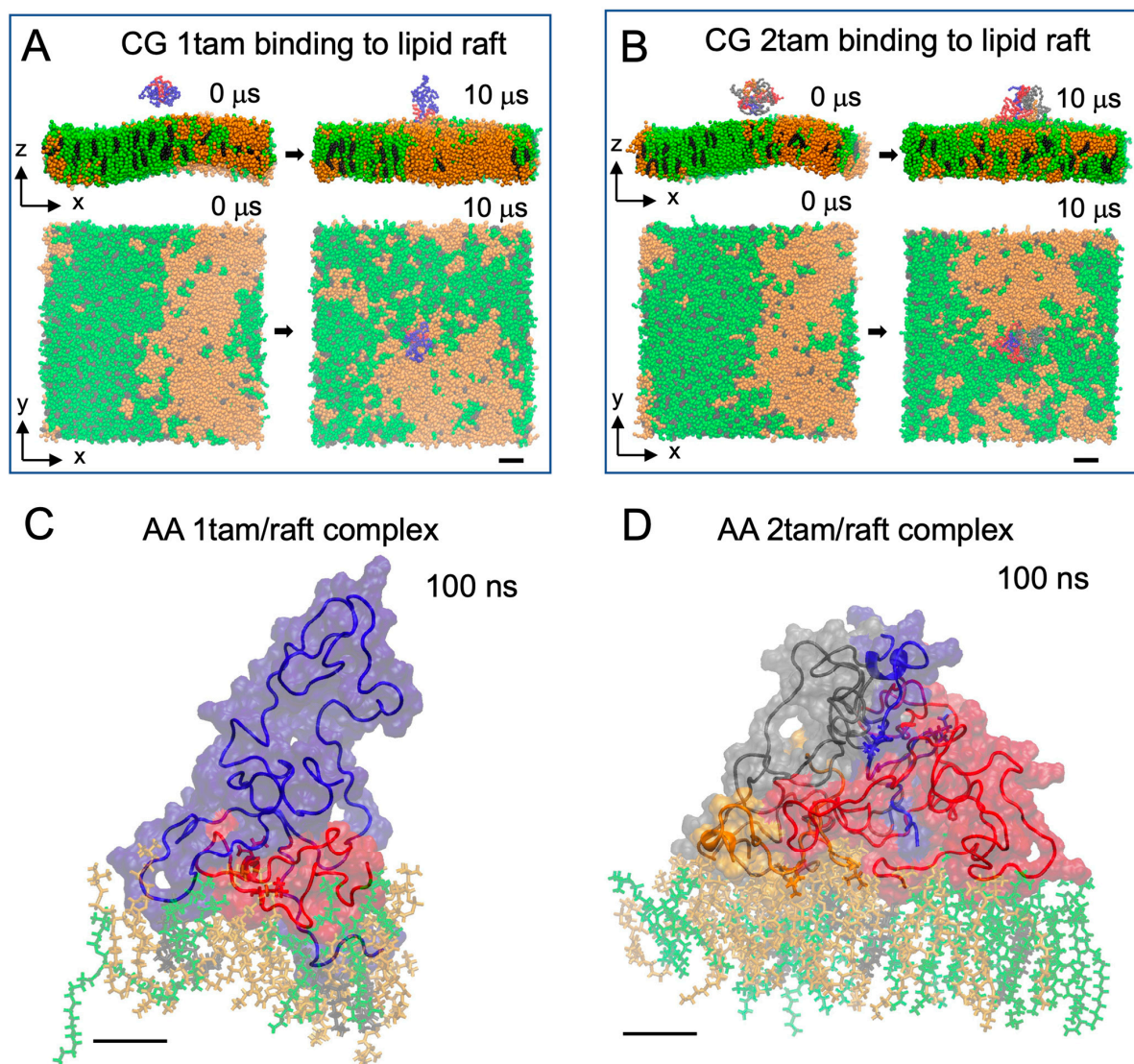


Figure 2. Modeling heterogeneous tau-amylin oligomer binding to the raft membrane. The initial ($0 \mu\text{s}$) and final membrane-bound ($10 \mu\text{s}$) CG structures of 1tam/raft (**A**) and 2tam/raft (**B**) complexes from representative replicates in both transverse (x - z) and lateral (x - y) views are shown. In the CG structures, the DPPC, DLPC, and CHOL are shown in green, orange, and black beads, and the protein structures are represented in a backbone ribbon form with chain A in blue, chain B in red, chain C in gray, and chain D in orange, respectively. A CG-to-AA spatial transformation step converted the $10 \mu\text{s}$ -structures of CG 1tam/raft and 2tam/raft complexes to the corresponding AA structures. Thereafter, 100 ns-long AA simulations were performed, and the final 100 ns structures of 1tam/raft (**C**) and 2tam/raft (**D**) complexes are shown. Other than the backbone ribbons, the colored AA protein surfaces of all the protein atoms are also given. The lipids are shown in licorice with identical color assignments as in the CG structures. All the CG and AA simulations were performed in 0.1 M NaCl and under physiological conditions of 1 atmosphere and 310 K. The two hydrophobic residues at L16 and I26 of the amylin chain in both 1tam and 2tam are shown in black. A scale bar of 1 nm is shown.

The same *g_select* tool was also used to characterize the annular lipid (AL) shell from each oligomer-raft complex upon protein binding. If an atom of any lipid was within 0.5 nm from an atom of an oligomer, that lipid was assigned to the AL shell. The non-annular lipid (nAL) region was also classified. This nAL region contains lipids that are outside the AL lipid shell. The details of AL and nAL lipid assignments are described in detail elsewhere [26].

2.5. Membrane Binding Behaviors of Oligomers

The membrane binding behaviors, in terms of the lipid-binding kinetics and protein residue-resolved, lipid-, or water-binding regions, of the oligomers were investigated using a minimum-distance analysis tool, *mindist*, from GROMACS [19]. Briefly, the time-dependent information of protein-lipid or protein-water minimum distance (*mindist*), defined as the minimum distance between any protein atom and the atom of its binding lipid or water neighbors, was recorded during the entire MD simulation. In addition, the number of contacts of the *mindist* within an interaction threshold (2 nm) vs. simulation time was also determined. Finally, the time-averaged *mindist* vs. protein residue number over the stabilized membrane binding event of the CG simulation or the last 50 ns of the AA simulation was calculated. These three parameters, *mindist* vs. time (upper panel), number of contacts vs. time (mid panel), and *mindist* vs. protein-residue number (bottom panel) are presented as a 3-panel plot of each replicate. Detailed procedures of the *mindist* analysis are described elsewhere [15,26].

2.6. Characterizations of Disruptions of Lipid Orientational Order by Membrane-Bound Oligomers

To evaluate the spatially resolved protein-induced membrane lipid structural order disruption by the membrane-bound oligomer, the lipid orientational order parameter of the lipids in the AL shell or the nAL region as a function of the carbon number of each lipid acyl chain, i.e., *sn-1* and *sn-2*, was systematically calculated using the *order* tool of GROMACS [19]. This calculated lipid order parameter is a measurement of the tilt of three sequentially connected carbon atoms along the PC acyl chains with respect to the normal of the bilayer, and therefore, provides a transverse (along the bilayer normal) profile of the lipid acyl chain ordering in the AL shell surrounding the membrane-bound protein and in the nAL region (control). Similarly, the orientational order of the rigid fused rings of CHOL was also determined in the AL shell and the nAL region. The time- and replicate-averaged values of the lipid order parameters of DPPC, DLPC, and CHOL across the last 50 ns of the simulations and from three independent replicates were systematically determined. Details of the membrane disruption characterization of the lipids in the AL and nAL shells in the lipid membrane have been given elsewhere [26].

2.7. Secondary Structures of Membrane-Bound Oligomers

The residue-resolved secondary structure of the membrane-bound oligomer at every time step was calculated from the AA simulation using the tool, *do_dssp*, from GROMACS [19] based on the Define Secondary Structure of Proteins (DSSP) algorithm [32]. To streamline surface-induced protein folding analysis, we grouped the beta-sheet and beta-bridge structures into a single "beta" group, and the three helical structures, alpha helix (A-helix), p-helix (or 5-Helix), and 310 helix (3-Helix), into a single "alpha" group. The time- and replicate-averaged numbers of amino acid residues of the protein in each secondary structure group, beta, alpha, turn, and random, were calculated over the last 50 ns and across all three replicates for each membrane-bound oligomer in the raft membrane.

2.8. Protein-Residue Contact Maps of Membrane-Bound Oligomers

To evaluate the interactions between residues from different types of proteins within the hetero-oligomer, 3D protein residue contact maps describing the color-coded residue-residue minimum distances among all the protein residues along the *x*- and *y*- axes were calculated using the tool, *g_mdmat*, from GROMACS [19] and a statistical and molecular

interaction analysis tool, CONAN [33]. Time-averaged protein residue contact maps with standard deviation were generated. Details of residue contact map generation were described in our previous studies [15,26].

3. Results

Using both CG and AA simulations, we aimed to explore the lipid binding, membrane disruption, and protein-folding events of the hetero-oligomers on phase-separated raft membranes. These events were compared with those from the homo-tau and -amylin oligomers.

3.1. Lipid Binding Kinetics of Hetero-Oligomer Binding to the Raft Membrane

In addition to the qualitative VMD visualization of the oligomer binding to the raft membrane, minimum distance (*mindist*) analysis (see Section 2) based on a three-panel *mindist* plot format was employed to examine the detailed binding kinetics of 1tam and 2tam in the raft membrane.

The top panels of Figures 3A and 4A demonstrate the protein–lipid *mindist* vs. time plots for the 1tam/raft and 2tam/raft complexes from 0 to 10 μ s of the CG simulations, respectively, from replicate 3 of each complex. Large fluctuations in the *mindist* values from 0 to 2.8 μ s and 0 to 3.8 μ s followed by stable *mindist* values of \sim 0.5 nm were evident in the 1tam/raft and 2tam/raft complexes, respectively. The large fluctuating *mindist* values indicate that the oligomer stayed in the solution phase, but made transient contact with the membrane surface. On the other hand, stabilized *mindist* values around 0.5 nm indicate that the oligomer was in a stable membrane-bound state. Here, the time of transition from fluctuating to stabilized *mindist* values at 2.8 or 3.8 μ s is defined as the lipid-binding time of the 1tam or 2tam to the raft membrane, respectively, and agrees with the qualitative VMD visualization results (see Section 2).

Other than the protein–lipid *mindist* vs. time plots, the number of contacts between protein and lipid atoms within 2 nm vs. time plots were also used to investigate the oligomer-to-membrane binding kinetics. As demonstrated in the mid panels of Figures 3A and 4A, the number of contacts showed a transition from near zero to large values at 2.8 and 3.8 μ s, signifying the establishment of contact between the protein and lipid atoms for 1tam and 2tam, respectively, and the results agree perfectly with the lipid-binding times revealed by the *mindist* vs. time plots (top panels), as described above.

Using the above *mindist* and the number of contacts vs. time analytical approaches, the lipid binding times for replicate 1 and replicate 2 of the 1tam/raft complex were detected at 0.2 and 2.2 μ s, respectively, as shown in Figure S2A,B. For the 2tam/raft complex, the lipid binding times were 1.1 and 11.1 in replicates 2a and 2b, respectively, as shown in Figure S3A,B. As mentioned in Section 2, two independent membrane-binding events were detected in replicate 2.

3.2. Lipid Binding Patterns of Hetero-Oligomers

The protein residue-resolved binding patterns of hetero-oligomers in the raft membrane were investigated. The time-averaged *mindist* vs. protein residue number over the stable membrane binding interval (see Section 2), or *mindist* spectrum, was calculated for each independent membrane binding event of the 1tam/raft and 2tam/raft complexes. Here, both the protein–lipid and protein–water minimum distances were determined. The lower panels of Figures 3A and 4A demonstrate the *mindist* spectra of the 1tam/raft and 2tam/raft complexes, respectively, from replicate 3 of each complex based on the CG simulations. The CG *mindist* spectra of other replicates are given in Figures S2 and S3. Since each hetero-oligomer contains multiple peptide chains of tau and amylin, the accumulated residue numbers, i.e., 1–130 and 131–68, were used to identify the tau (chain A) and amylin (chain B) for the dimeric 1tam. For the tetrameric 2tam, the residue numbers 1–37, 38–167, 168–297, and 298–334 were used to identify the amylin (chain A), tau (chain B), tau (chain C), and amylin (chain D), accordingly. Significant dips, or local minima, of the protein–lipid

mindist spectra of 1tam and 2tam were evident. In addition, distinct peaks of protein–water *mindist* spectra were also detected.

Mindist analysis of 1tam binding to the raft membrane

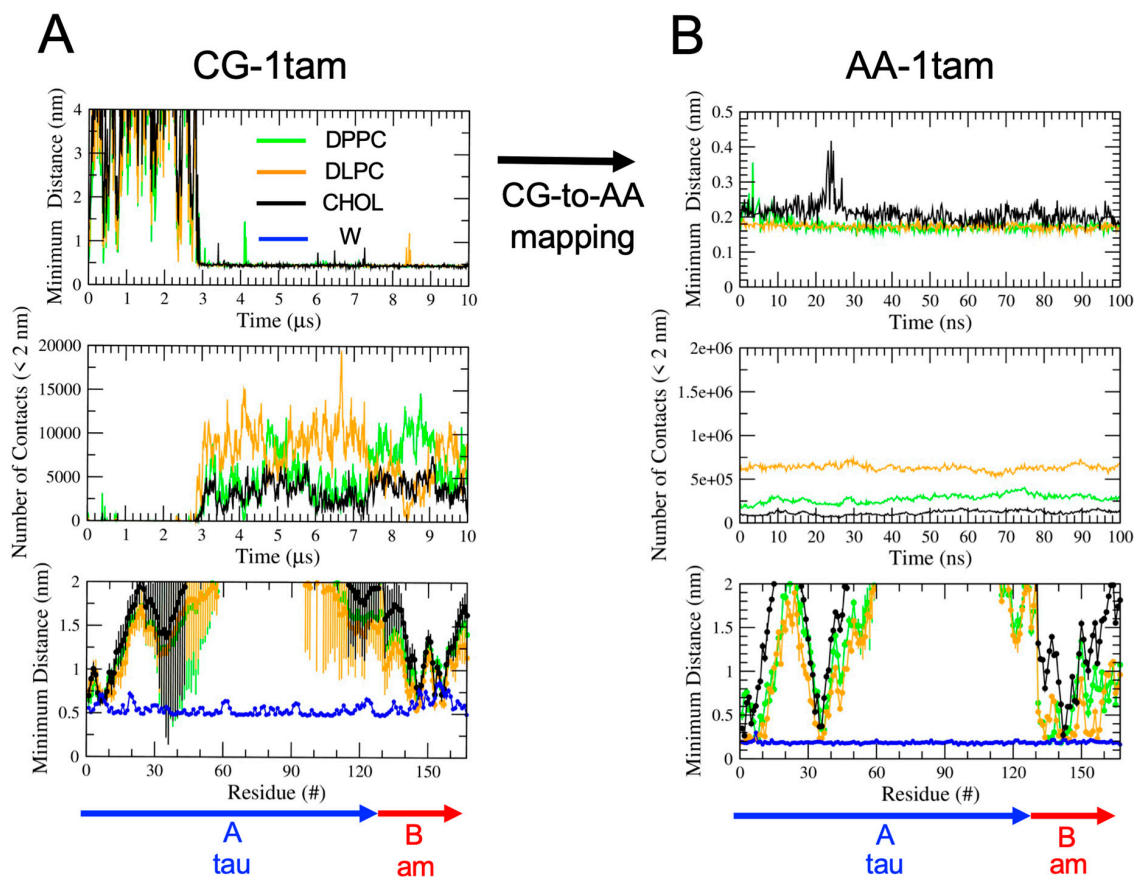


Figure 3. Minimum distance analysis of 1tam binding to the raft membrane. Two three-panel plots of the minimum distance (*mindist*) between protein and lipid (or water) atoms (*mindist*) of replicate 3 of 1tam/raft complex in a 10- μ s-long CG (A) and a 100-ns-long AA (B) AA simulation are shown. The initial structure of the AA simulation was obtained from the 10 μ s CG structure after a CG-to-AA spatial transformation step. The upper panel shows the *mindist* between protein and lipid atoms vs. time, and the middle panel shows the number of contacts within 2 nm between protein and lipid atoms vs. time. The lower panel shows the time-averaged *mindist* between protein and lipid (or water) atoms vs. protein residue # over the last 5 μ s for CG (A) and the last 50 ns for AA (B). All *mindist* values are color-coded based on the lipid types; DPPC is shown in green, DLPC is shown in orange, CHOL is shown in black, and water is shown in blue. The error bar represents the standard deviation of the mean. The protein residue locations of the tau and amylin (am) chains inside the 1tam are identified by the blue (chain A) and red (chain B) arrows, respectively.

The above three-panel *mindist* analysis was also applied to the CG-to-AA converted structures, as demonstrated in Figures 3B and 4B for the 1tam/raft and 2tam/raft complexes, respectively, for replicate 3 of each complex. The *mindist* or numbers of contact plots of the AA structures did not show any abrupt changes in contrast to the abrupt transitions observed in the CG structures. These observations suggest that the oligomer remained bound to the raft surfaces throughout the entire AA simulation. Also, the AA protein–lipid *mindist* spectra showed similar binding patterns, or the locations of the local dips, when compared with the CG *mindist* spectra, suggesting similar protein–lipid binding patterns of the membrane-bound oligomer in both the CG and AA structures. Figures S2 and S3 show

the AA *mindist* spectra of the other replicates. Note that the absence of large fluctuations during the 100 ns-long AA simulations simply implies that the protein remains attached to the raft membrane surface after the microsecond-long CG simulations. There is no guarantee that either the 10 μ s-long CG or 100 ns-long AA represents a stable protein–membrane event. Much longer CG and AA simulations are needed to ensure stable protein–membrane binding behaviors.

Mindist analysis of 2tam binding to the raft membrane

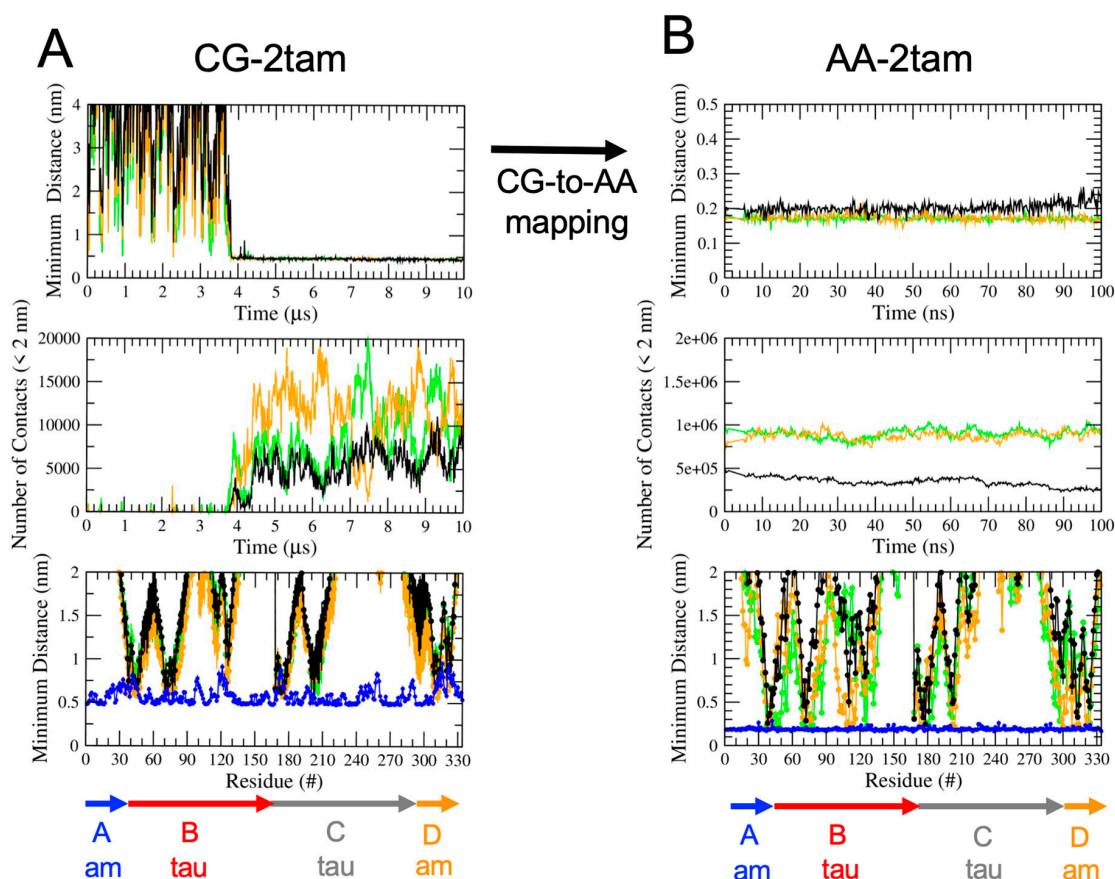


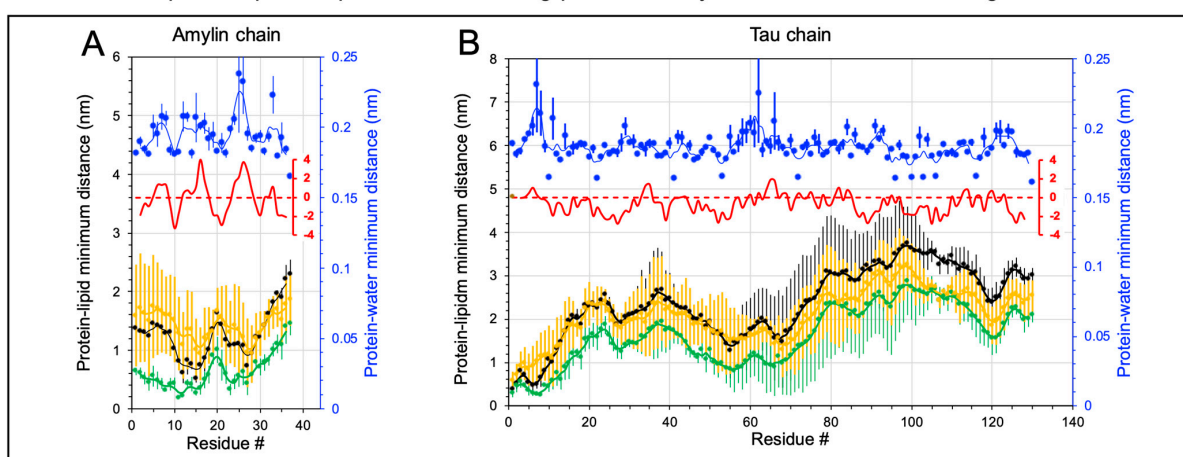
Figure 4. Minimum distance analysis of 1tam binding to the raft membrane. Two three-panel plots of the minimum distance (*mindist*) between protein and lipid (or water) atoms (*mindist*) of replicate 3 of 1tam/raft complex in a 10- μ s-long CG (A) and a 100-ns-long AA (B) AA simulation are shown. The initial structure of the AA simulation was obtained from the 10 μ s CG structure after a CG-to-AA spatial transformation step. The upper panel shows the *mindist* between protein and lipid atoms vs. time, the middle panel shows the number of contacts within 2 nm between protein and lipid atoms vs. time. The lower panel shows the time-averaged *mindist* between protein and lipid (or water) atoms vs. protein residue # over the last 5 μ s for CG (A) and the last 50 ns for AA (B). All *mindist* values are color-coded based on the lipid types; DPPC is shown in green, DLPC is shown in orange, CHOL is shown in black, and water is shown in blue. The error bar represents the standard deviation of the mean. The protein residue locations of the tau and amylin (am) chains inside the 2tam are identified by the blue, red, gray, and orange arrows, corresponding to chains A (am), B (tau), C (tau), and D (am), respectively.

To evaluate the stability of the protein–lipid binding pattern, Figures S4 and S5 show the protein–lipid and protein–water *mindist* heatmaps, i.e., the color-coded *mindist* values vs. protein residue number (column) and time of simulation (row), for all the replicates of the AA simulations of 1tam/raft and 2tam/raft complexes, respectively. Stable protein–

lipid and protein–water binding patterns were evident in both the 1tam/raft and 2tam/raft complexes throughout the entire 100 ns AA simulations in all six independent replicates.

A careful examination of the *mindist* spectra in Figures S2 and S3 revealed that the single amylin (chain B) of the 1tam bound to the raft membrane around the L16 and I26 residues. However, only one of the two amylin chains (chain A or D) of the 2tam bound to the raft membrane at similar residue locations. For the tau (chain A in 1tam or chains B and C in 2tam), the regions around the *N*-terminal, I35, and I66 were the major lipid binding sites. Figure 5A,B shows the time- and replicate-averaged *mindist* spectra of the constituent amylin chain and the constituent tau chain, respectively, from the last 50 ns of the AA simulation and across three independent replicates of the 1tam/raft. Similarly, Figure 5C,D shows the time- and replicate-averaged *mindist* spectra of the 2tam/raft complex. Since only one of the two amylin chains bound to the raft membrane, these membrane-associated amylin chains were used in the calculation of the *mindist* spectra of the 2tam/raft complexes.

Atomistic protein-lipid and protein-water binding profiles of amylin and tau chains in heterogeneous 1tam



Atomistic protein-lipid and protein-water binding profiles of amylin and tau chains in heterogeneous 2tam

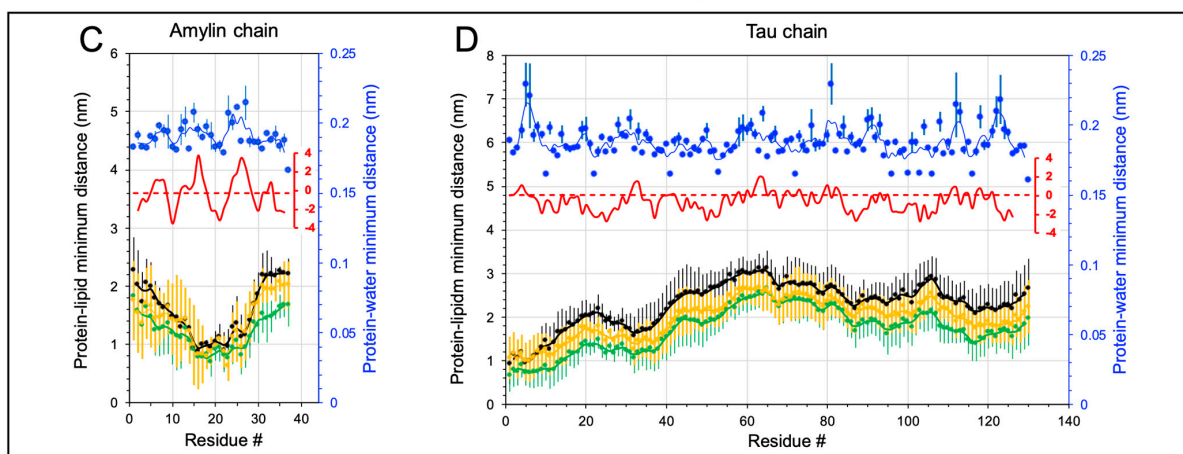


Figure 5. Minimum distance spectral analysis of tau–amylin oligomers in the raft membrane. The minimum distance (*mindist*) spectrum, defined as time-, replicate-, and chain-averaged minimum distance between protein and lipid (or water) vs. protein residue, for the 1tam/raft (A,B) and 2tam/raft (C,D) complexes. Each data point represents the average over the last 50 ns, across three replicates, and over the constituent chain (amylin or tau). The error bar represents the standard error of the mean. The *mindist* values are color-coded, with DPPC shown in green, DLPC shown in orange, CHOL shown in black, and water shown in blue. The hydrophobicity plot is given in red (see Section 2) to facilitate the identification of the hydrophobicity residues in each chain. A 5-point moving-average fit is presented for the *mindist* spectral plots.

In the averaged *mindist* spectra of amylin, two well-resolved dips at ~L16 and I26 were evident for the 1tam/raft complex. In contrast, a broad dip from L16 to I26 was found for the 2tam/raft complex. Interestingly, two major protein–water peaks at L16 and I26 were clearly detected for both the 1tam/raft and 2tam/raft complexes. In the averaged *mindist* spectra of tau, a major minimum at the *N*-terminal was evident for both the complexes. Also, a broad minimum at around I66 or I35 was detected in the 1tam/raft or 2tam/raft, respectively. Again, the locations of the above minima of the protein–lipid *mindist* spectra agreed with those of the peaks of the protein–water *mindist* spectra, particularly for the peaks at the *N*-terminal and I66. Hence, the L16 and I26 residues of amylin and the *N*-terminal of tau represent the common and major membrane-binding sites of 1tam and 2tam binding to the raft membrane.

3.3. Disruptions of Lipid Domain Sizes by Hetero- and Homo-Oligomers

The perturbation effects of the membrane-bound hetero-oligomers on the lipid domain sizes were investigated by measuring the lipid compositions of the three lipid domains (Lo, Ld, and Lod), and the results were compared with those of the homo-amylin (1am, 2am, and 4am) and -tau (1tau, 2tau, and 4tau) oligomers. Figure 6 shows the time- and replicate-averaged lipid % in the Lo, Ld, and Lod domains vs. the total amino acid number of each oligomer from the CG simulations. For the homo-amylin and -tau oligomers, the total amino acid numbers of 1am, 2am, 4am, 1tau, 2tau, and 4tau are 37, 74, 148, 130, 260, and 520, respectively. For the hetero-oligomers, the total amino acid numbers of 1tam and 2tam are 167 and 334, respectively. Also, the lipid compositions of the lipid domains in the absence of oligomers (controls) are given. Note that the sum of DPPC and DLPC % in the Lod domain is labeled as Lod-PC (see Section 2).

In the absence of oligomers, the compositions of CHOL were ~64, 11, and 25% in the Lo, Ld, and Lod domains, respectively. On the other hand, the compositions of Lo-DPPC, Ld-DLPC, and Lod-PC were ~28, 9, and 63% in the Lo, Ld, and Lod domains, respectively. Except for the dimeric oligomers, i.e., 2am, 2tau, and 1tam, the CHOL and PC % were found to decrease in the Lo domain (Figure 6A,D), but increase in the Lod domain (Figure 6C,F) when compared with those of the controls. Interestingly, the lipid % of all the lipid types remained the same in the Ld domain (Figure 6B,E) in the presence or absence of all the types of oligomers.

3.4. Characterizations of Annular Lipids Surrounding the Hetero- and Homo-Oligomers

To examine the local membrane disruptive effects of membrane-bound oligomers, the annular lipids surrounding each membrane-bound oligomer were identified (see Section 2). Figure S6 shows the time- and replicate-averaged numbers and percentages of DPPC, DLPC, and CHOL in the AL shell over the last 50 ns of the AA simulations and across three independent replicates of the hetero- and homo-oligomers. We observed that the number of lipids in the AL shell increased steadily with the total amino acid number of the protein for the AL-CHOL and AL-DPPC. In contrast, these values remained relatively constant at ~10 for the AL-DLPC. As a result, the percentages of CHOL, DPPC, and DLPC in the AL shell were ~20, 35, and 45% for the homo-amylin oligomers and ~30, 45, and 25% in the homo-tau oligomers or hetero-oligomers, respectively. Therefore, DPPC represented the major lipid type in the AL shell of the homo-tau or hetero-oligomers. In contrast, DLPC was the major lipid type in the AL shell of the homo-amylin oligomers.

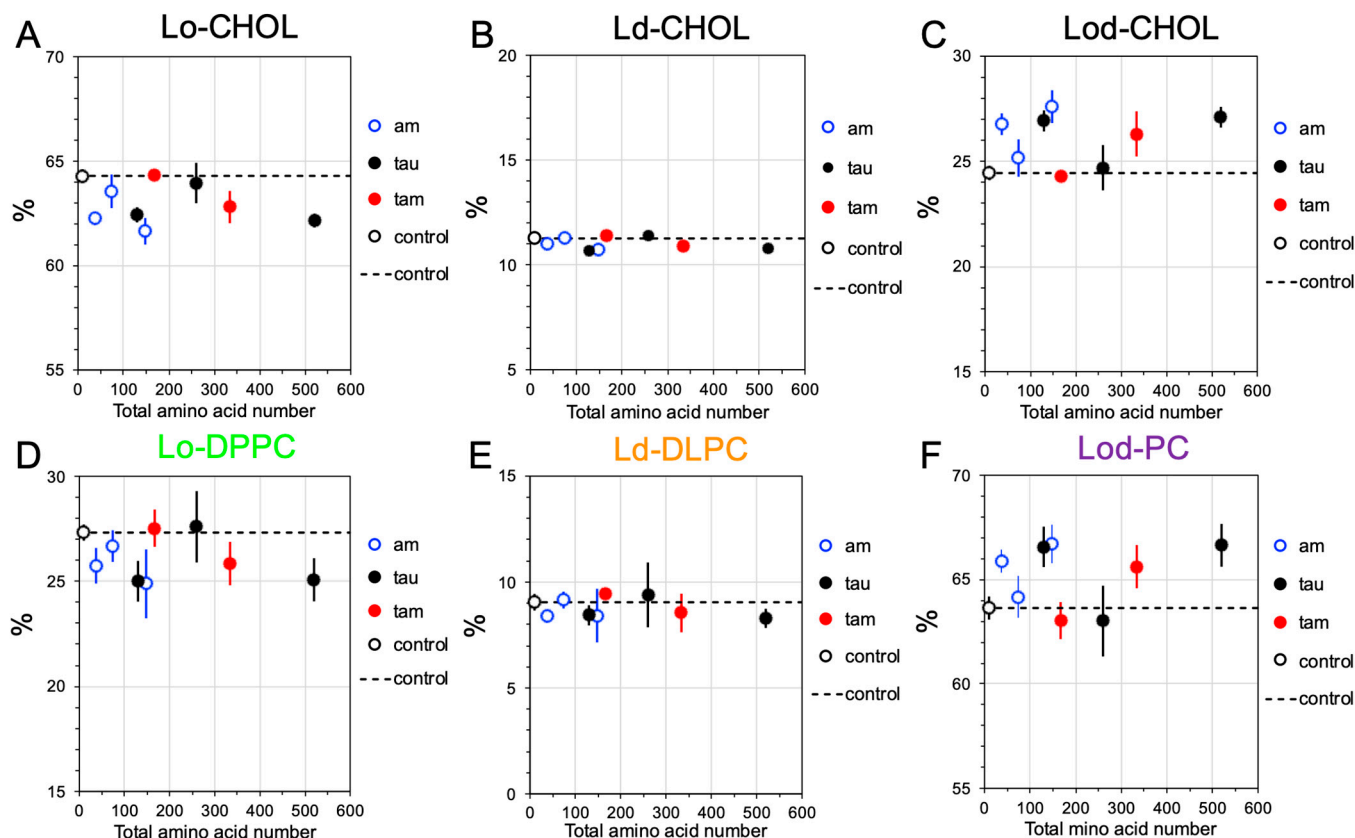


Figure 6. Lipid domain disruption by oligomers in the raft membrane. Plots of the percentages of CHOL in the Lo (A), Ld (B), and Lod (C) domains, and those of DPPC in the Lo domain (D), DLPC in the Ld domain (E), and the sum of DPPC and DLPC, or PC, in the Lod domain (F) vs. the total amino acid number of each oligomer are shown. Each percentage data point represents the time- and replicate average over the time interval of stable membrane binding and across three independent replicates. Both homo-amylin oligomers (1am, 2am, and 4am), homo-tau oligomers (1tau, 2tau, and 4tau), and hetero-oligomers (1tam and 2tam) are shown in blue circles, filled black circles, and filled red circles, respectively. The control represents the percentage data in the absence of protein. The oligomers are placed in the plot according to their total amino acid numbers. The error bars are standard errors of the means.

3.5. Disruptions of Orientational Orders of Annular Lipids by Hetero- and Homo-Oligomers

The extent of disruption of the orientational order of the acyl chains in the AL shell was investigated for each hetero-oligomer, and the result was compared with that for the homo-oligomer.

Since each PC has two acyl chains, i.e., *sn*-1 and *sn*-2 chains, the order parameter vs. carbon number plots, or order profiles, of both chains were calculated separately, for all the oligomers. As a control, the order profile of the lipids in the nAL region for each oligomer is also shown. The order profiles of DPPC and DLPC in the AL shell for the hetero-oligomers are shown in Figure 7. In general, the order profile of the *sn*-2 chain of either DPPC or DLPC was lower than that of the *sn*-1 chain as expected since the *sn*-2 chain is closer to the membrane surface than the *sn*-1 chain. For the hetero-oligomer, the disruptions of the DPPC lipid profile over the first eight carbons caused by the dimeric 1tam (Figure 7B) were much stronger than those caused by the tetrameric 2tam (Figure 7F). Yet, no significant difference was evident for the DLPC lipid profile (Figure 7D vs. Figure 7H).

Phospholipid order disruption effects of heterogeneous tau-amylin and homogeneous tau oligomers

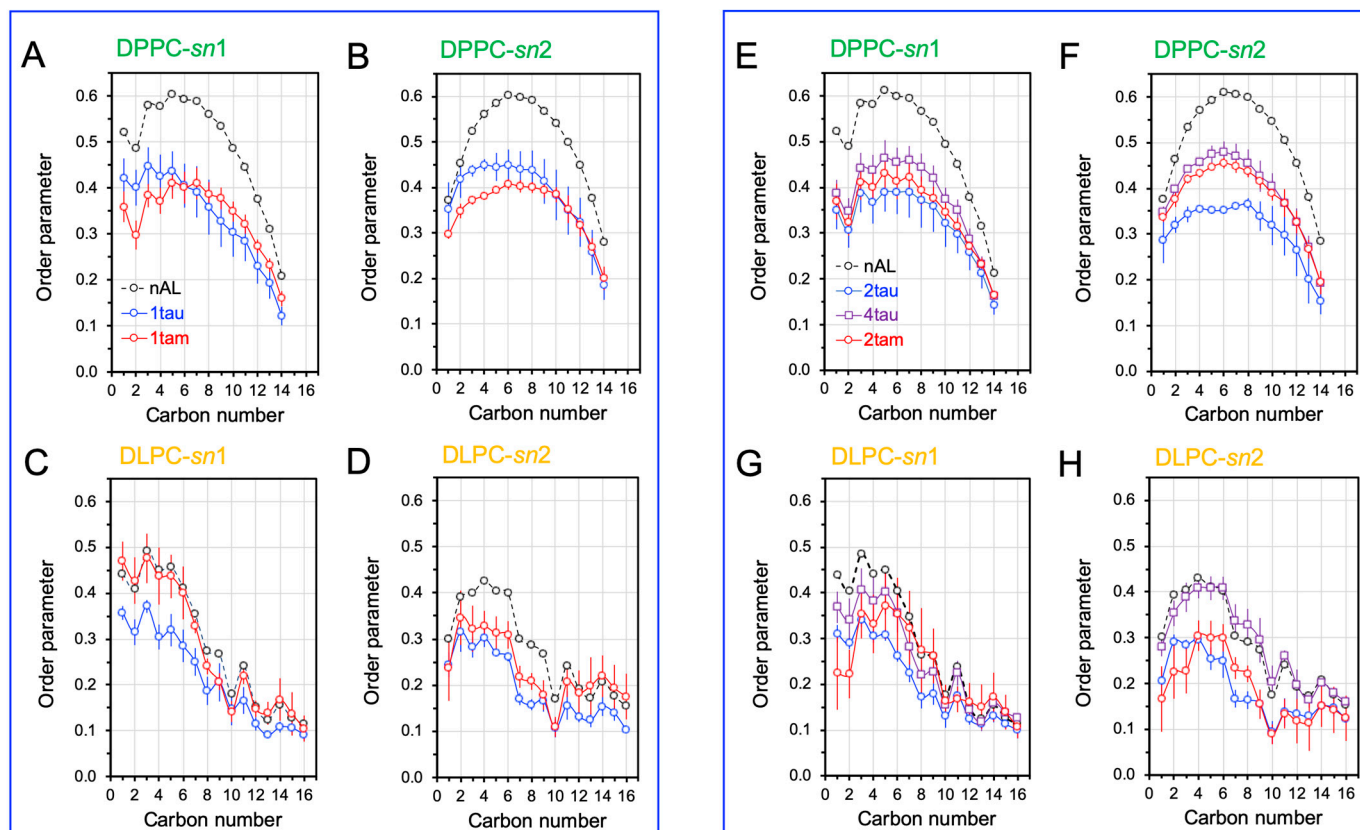


Figure 7. Phospholipid order disruptions by hetero- and homo-tau oligomers. The time- and replicate-averaged plots of the phospholipid orientational order parameter vs. lipid acyl chain carbon number, or order profiles, over the last 50 ns of the AA simulation and across all replicates, for DPPC (A,B,E,F) and DLPC (C,D,G,H) in the 0–0.5 nm annular lipid (AL) shell of the hetero-oligomers (1tam and 2tam) and homo-amylin oligomers (1tau, 2tau, and 4tau) are shown. The lipid profiles of the lipids outside the AL shell, or non-annular lipids (nAL), are also shown as controls. The data points for the *sn*-1 (A,C,E,G) and *sn*-2 (B,D,F,H) chains are presented. The error bar indicates the standard error of the mean for each data point.

The disruptions of PC order profiles caused by the hetero-oligomers were directly compared with those caused by the homo-tau-oligomers. In DPPC, the order parameter profile for the 1tam was significantly lower than that for the 1tau in the first four carbon numbers, or near the PC headgroup, as shown in Figure 7A,B for the *sn*-1 and *sn*-2 chains, respectively. However, in DLPC, the trend was reversed as shown in Figure 7C,D, accordingly. For larger oligomers, the disruption of DPPC order profile caused by 2tau was significantly greater than that caused by either 2tam or 4tau over the carbon numbers 2–10 in the *sn*-2 chain (Figure 7F), but less so in the *sn*-1 chain (Figure 7E). In contrast, the disruption of DLPC order profile by the 2tam was large, while it was very similar to that caused by 2tau (Figure 7H) in the *sn*-2 chain. Relatively less-disruptive effects caused by 2tam, 2tau, and 4tau were found in the *sn*-1 chain (Figure 7G).

Similar comparisons of the disruptions of PC order profiles caused by the hetero-oligomers with those caused by the homo-amylin oligomers were performed, and the results are shown in Figure S7. In DPPC, the disruption of the order profile caused by 1tau was significantly greater than that caused by 1am over the first five carbon numbers in both the *sn*-1 and *sn*-2 chains (Figure S7A,B). Yet, no significant disruptions of the DPPC order profiles were found in both chains of DLPC (Figure S7C,D). For the larger oligomers, all oligomers (2tam, 2am, and 4am) reduced the DPPC order profile by a similar amount, e.g., with a decline of 16% at the eighth carbon for both the *sn*-1 (Figure S7E) and *sn*-2

(Figure S7F) chains. In DLPC, the disruption of the order profile caused by 2tam was much greater than that caused by either 2am or 4am in both the *sn*-1 (Figure S7G) and *sn*-2 (Figure S7H) chains.

The CHOL ring order parameters (see Section 2), or defined as the CHOL order, of the AL and nAL for all the oligomers were also determined, and the results are shown in Figure 8. Overall, the values of CHO order were around 0.5 for all the oligomers, except for the 2tam of ~0.4, which was significantly smaller than that for 1 tau or 2tau, but not much for the 4tau, suggesting strong disruption of CHO order caused by 2tam when compared with that of most homo-oligomers.

CHOL order disruption effects of heterogeneous tau-amylin and homogeneous tau or amylin oligomers

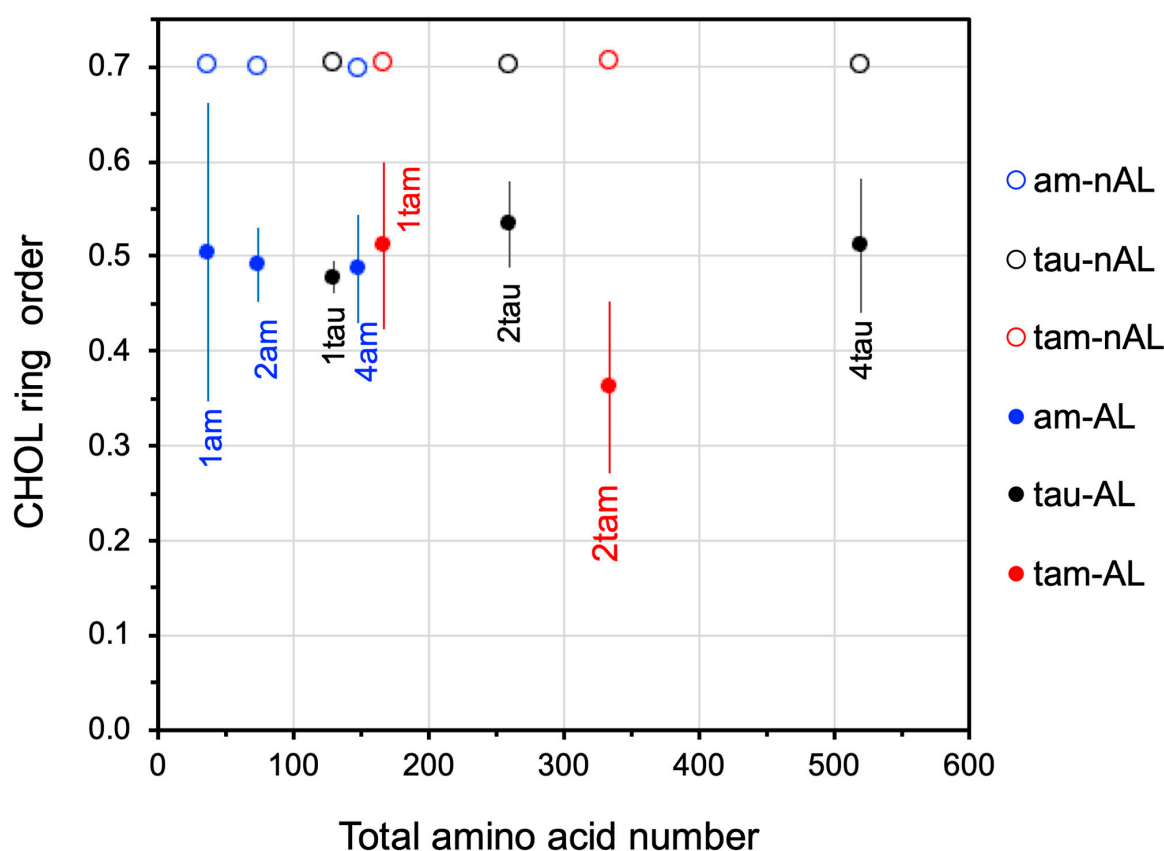


Figure 8. Membrane cholesterol order disruptions by hetero- and homo-oligomers in the raft membrane. The time- and replicate-averaged plots of the cholesterol (CHOL) orientational order parameter over the last 50 ns of the AA simulations and across all replicates, in the 0–0.5 nm annular lipid (AL) shells of the hetero-oligomers (1tam and 2tam), homo-tau-oligomers (1tau, 2tau, and 4tau), and homo-amylin-oligomers (1am, 2am, and 4am) are shown. The oligomers are placed in the plot according to their total amino acid numbers. The error bar indicates the standard error of the mean for each data point.

3.6. Protein Folding of Hetero- and Homo-Oligomers on Raft Membrane Surfaces

The time- and residue-resolved protein secondary structures, or the DSSP profiles (see Section 2), of the membrane-bound hetero-oligomers were determined, and the results of the representative replicates for 1tam and 2tam are shown in Figure 9. For comparison, the representative DSSP profiles for the homo-amylin and -tau oligomers are shown in Figure S8. For the homo-oligomers, we observed that more beta-sheet structures were

found in the larger oligomers than those in the small oligomers. In addition, significant alpha-helix structures were found exclusively in the amylin oligomers, but not in the tau oligomers. For the hetero-oligomers, beta-sheet structures were evident in both 1tam and 2tam. Also, alpha-helix structures were again evident in the single amylin chain of 1tam and two amylin chains of 2tam. By combining the secondary structures into four major classes, i.e., beta, alpha, turn, and random (see Section 2), Figure 10C,D shows the fraction of each major secondary structure from the DSSP profile vs. time for the representative replicates. Here, ~3 and 8% of alpha and beta structures, respectively, were observed in both the replicates.

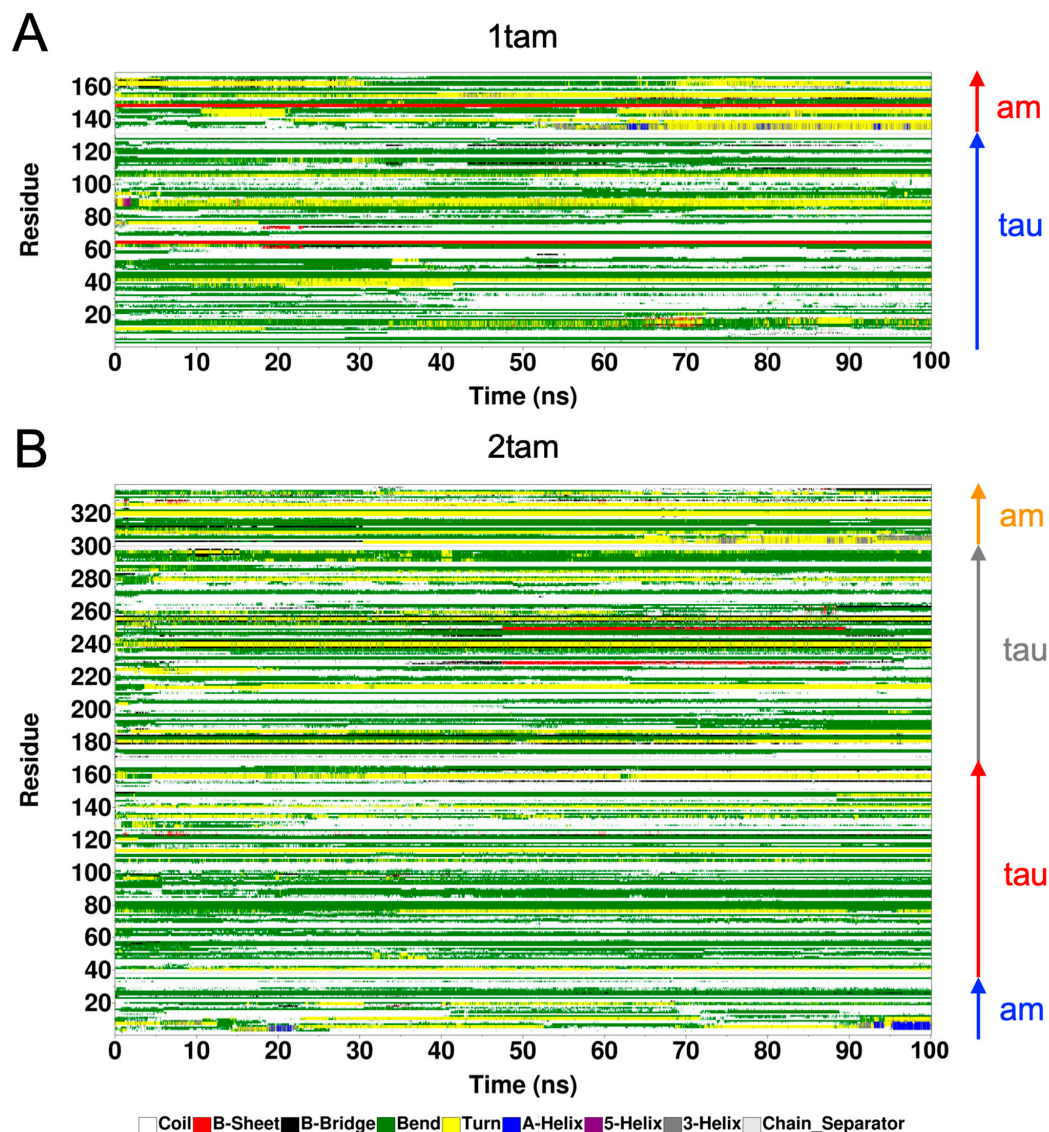
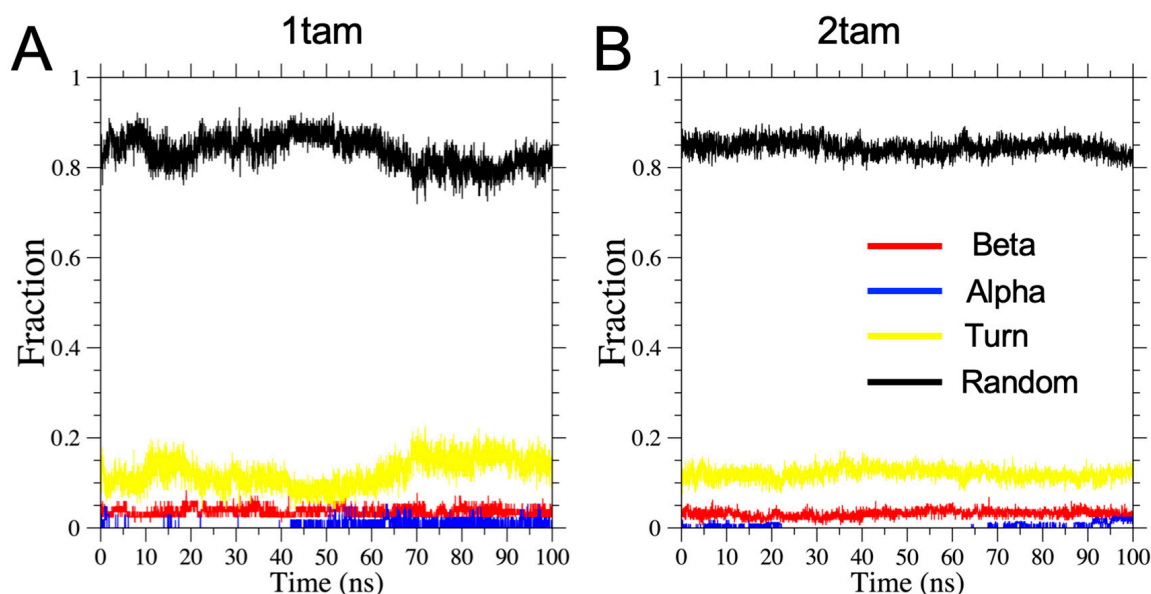


Figure 9. Time evolution of protein secondary structure of hetero-oligomers upon binding to the raft membrane. The 3D color-coded protein secondary structures as a function of residue number (vertical axis) and simulation time (horizontal axis) are presented in a DSSP format (see Section 2) for the representative replicates of 1tam (A) and 2tam (B) oligomer. The protein residue locations of the constitute tau and amylin (am) chains inside the hetero-oligomers are identified by the blue, red, gray, and orange arrows, respectively, and correspond to the chain A (tau) and chain B (amylin) for the membrane-bound 1tam, and chains A (am), B (tau), C (tau), and D (am), for the membrane-bound 2tam, accordingly.

Secondary structures of heterogeneous oligomers



Secondary structures of heterogeneous and homogeneous oligomers

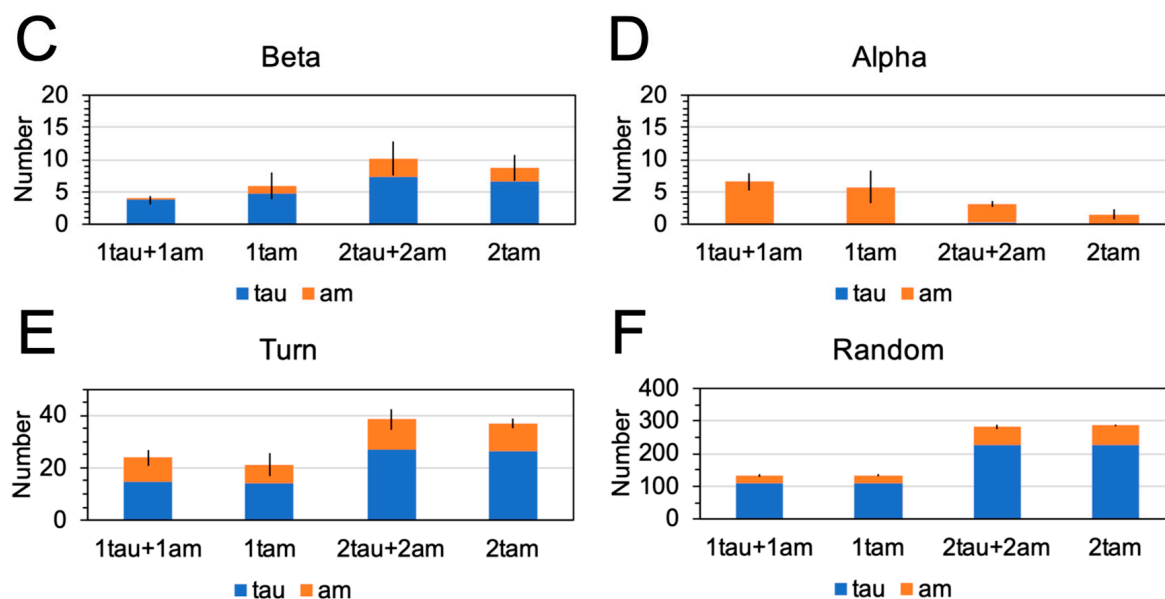


Figure 10. Protein secondary structures of membrane-bound hetero- and homo-oligomers. The fraction of protein residues that participated in four secondary structure groups, beta, alpha, turn, and random (see Section 2) vs. time of the representative replicates of the membrane-bound 1tam (A) and 2tam (B) from the AA simulations are demonstrated. The number of residues that participated in each secondary structure group was also calculated from each of the AA trajectories. Comparisons of the time-, replicate-, and chain-averaged secondary structure groups (C–F) over the last 50 ns across all three replicates and over the tau and amylin chains separately of oligomers are shown in stacked histograms. For the homo-oligomers, the sum of secondary structures from 1tau and 1am or 2tau and 2am are presented as a (1tau + 1am) or (2tau + 2am) group, and this sum is directly compared with the secondary structure of 1tam or 2tam, respectively. Note that the total amino acid number of (1tau + 1am) or (2tau + 2am) is 167 or 334 and matches with that of 1tam or 2tam, accordingly.

To reveal the effect of protein self-aggregation on the secondary structures of the constituent amylin and tau chains separately, we have directly compared the time- and replicate-averaged numbers of secondary structures of the tau and amylin chains in the homo-oligomers with those of the constituent tau and amylin chains in the hetero-oligomers. The data points from the last 50 ns of the AA were used for the time average. The comparisons are expressed in a stacked histogram format, as given in Figure 10. For the beta structure (Figure 10A), a small, but significant, beta structure was detected in the single amylin chain of the dimeric 1tam, but not in the 1am monomer alone. No significant difference in the beta structure was detected in either the tau or am chains in 2tam vs. the 2tau and 2am chains alone. Interestingly, alpha structures were exclusively found in the amylin chains, but not in the tau chains in both the homo- and hetero-oligomers, as shown in Figure 10B. Also, a decline in the alpha structures was evident for larger oligomers, i.e., 2tau, 2am, and 2tam, when compared with that of the smaller oligomers, i.e., 1tau, 1am, and 1tam. No significant differences in turn or random structures were found among the homo- and hetero- oligomers, as shown in Figure 10C,D.

3.7. Residue-Resolved Protein–Protein Contact Map

Using a statistical and molecular interaction analysis tool, CONAN (see Section 2), the residue-resolved protein–protein interactions at the interface between the amylin and tau monomers inside the hetero-oligomers were examined, as shown in Figure S9. It appears that the residues around the C-terminal of amylin interact strongly with mostly the middle region of the tau in both the hetero-dimer and -tetramer. Furthermore, the two monomeric amylin monomers did not make contact with each other in the hetero-tetramer (Figure S9B). Interestingly, the highly dynamic nature of the protein–protein residue contacts among the residues in the amylin–tau interfacial regions is evident in the standard deviation contact maps, as shown in Figure S9C,D.

4. Discussion

Using multiscale MD simulations, we have investigated the macromolecular interactions associated with the lipid binding behaviors, the protein-induced membrane damage, and the surfaced-induced protein folding of the hetero-oligomers vs. homo-oligomers on the phase-separated raft membrane.

We have created a hetero-tetramer by protein self-assembling or -aggregation in a solution involving two amylin and two tau monomers. Clearly, the other combinations of tau and amylin monomers, i.e., three amylin monomers and one tau monomer, or one amylin monomer and three tau monomers, can form a hetero-tetramer in a solution. Also, these alternative combinations of amylin and tau monomers might have very different membrane binding interaction and protein-folding behaviors than the two amylin and two tau combination in this pilot study. More work is needed to explore these alternative combinations since multiple combinations of amylin and tau-monomers are likely to exist in an experimental setting. On particular interest is how the presence of three amylin may improve the binding affinity of the hetero-tetramer when compared with the presence of two amylin, since amylin has more specific and stronger lipid binding sites than tau. Other than different amylin and tau combinations in the hetero-tetramer, future studies on hetero-trimer consisting of multiple combinations of amylin and tau monomers will be of great interest to explore the hetero-oligomer interactions with the raft membrane.

Among three distinct lipid domains, Lo, Ld, and Lod, of the raft membrane, we discovered that the hetero-oligomers of all sizes preferentially bind to the Lod domain, as revealed by three-panel *mindist* analysis. Here, Lod represents the phase boundary region between the ordered Lo and the disordered Ld domains in the raft membrane. Interestingly, this finding is in line with recent computational studies on homo-oligomers involving beta-amyloid [26], tau [14], and amylin [15], which are all based on the same raft membrane. Besides amyloid oligomers, the other membrane-active proteins, such as HIV-*gp42* fusion protein and certain antimicrobial peptides [34–36], have also been found to bind to this Lod

domain region. It is believed that the line tension at the highly dynamic, phase domain boundaries or lipid packing defects due to the lipid bilayer thickness mismatch between the thicker L_{od} and the thinner L_d drives these membrane-active proteins to the dynamic L_{od} region [27,37,38]. Furthermore, a recently proposed elastic model [39] predicts that the L_{od} phase boundary serves as a universal attractor to regulate protein lateral sorting and affects the enrichment of membrane inclusions in the phase-separated membrane. Therefore, the L_{od} domain may represent a common lipid nanodomain region for some non-amyloidogenic and amyloidogenic proteins to bind to. In addition, the L_{od} domain may represent a unique biophysical-based membrane target for future drug interventions for preventing toxic and membrane-active protein attachment to the host cell membranes. Additional experimental and computational investigations are needed to further explore the macromolecular mechanism of protein/L_{od} binding and how it affects the subsequent protein-induced membrane damage.

Our results reveal that the hydrophobic residues L16 and I26 of amylin and the N-terminal of tau are the common and major membrane-anchoring sites of hetero-oligomers. Note that these results agree with those of homo-amylin [15] and homo-tau [14] oligomers on the raft membrane. Therefore, our current results suggest that the formation of a hetero-oligomer from tau and amylin retains the lipid binding specificities or patterns of membrane-binding domains of either a tau- or amylin-containing homo-oligomer.

The binding efficiency of the smaller hetero-dimer 1tam was greater than that of the larger hetero-tetramer 2tam. Interestingly, all three replicates of the 1tam/raft complex bound firmly to the membranes, while only two out of three replicates of the 2tam complex did. In addition, for the hetero-tetramer containing two chains of amylin and two chains of tau, we observed that only one of the two amylin chains was attached to the membrane. This can be due to the nature of the different attachment sites of the two amylin proteins on the surfaces of the neighboring tau proteins. Interestingly, our recent study shows that strong membrane binding via the L16 and I 26 residues of amylin was evident for the homo-amylin of all sizes [15]. Therefore, if a membrane-bound and stable dimeric amylin can form in the tetrameric 2tam, we should expect the stronger and more efficient membrane-binding of 2tam. However, we failed to observe such a structure in our self-assembling 2tam oligomers in a solution. This suggests that for larger hetero-oligomers the constituent amylin protein may protrude outside the membrane surface, making it more susceptible to refolding in a non-membrane environment.

We observed significant protein-induced membrane damage caused by the membrane-bound hetero-oligomers in terms of the raft domain lateral organizations across the entire raft membrane. The binding of the tetrameric 2tam strongly disrupted the raft organization by decreasing the amounts of DPPC and CHOL in the L_o domain and concomitantly increasing the boundary L_{od} domain. The extent of L_o domain disruption by the 2tam was comparable to that by the homo-oligomers, suggesting that the large hetero-oligomers have a strong lipid domain disruption effect on the raft membrane like the homo-oligomers of similar sizes.

For the local disruption effects of hetero-oligomers, we discovered that the perturbation effects of lipid order profiles by the membrane-bound oligomer depend on the oligomer size, the makeup (homo- vs. hetero) of the oligomers, and the lipid type. Saturated DPPC and CHOL are the major lipid constituents of the highly ordered L_o or raft domain, which is important in regulating the normal physiology of various membrane events, such as signal transduction or protein sorting [22]. Here, we observed that both dimeric 1tam and tetrameric 2tam disrupt the order profile of DPPC to a similar extent, suggesting the membrane disruption by hetero-oligomer is oligomer-size-independent for the raft membrane. However, we observed that the DPPC order disruption effect by the dimeric 1tam was much stronger than either 1am or 1tau, indicating the presence of amylin or tau in the 1tam promotes the lipid perturbation than either the amylin or tau monomer alone. On the other hand, the lipid order disruptive effects of the larger tetrameric 2tam were similar or even lower than those of the homo-amylin or -tau oligomers of similar

sizes. For cholesterol, the other major building block of the raft domain, the 2tam disrupted the CHOL ring order the most than any other hetero- or homo-oligomers, even the largest tetrameric tau oligomer, suggesting that the hybrid tau–amylin surfaces in the 2tam perturbs the CHOL orientation more effectively than the homo-tau-tau and -amylin-amylin surfaces in the homo-oligomers.

We observed significant surface-induced protein folding from the highly disordered structures in the solution to partially ordered membrane-bound structures for both homo- and hetero-oligomers. The previous studies have indicated that amylin forms an alpha-helix structure first and a beta-sheet structure later in a membrane environment [40–42]. The newly formed beta-sheets may create beta-sheet-enriched ion pores that disrupt the membrane functions, as suggested by various computational and experimental investigations [43–45]. For both the homo- and hetero-oligomers, we discovered that alpha-helix structures were mostly associated with the amylin, but not with the tau. In addition, we observed that the alpha-helix decreased drastically, with a concomitant increase in the beta-sheet structure as the oligomer size increased from a monomer to a tetramer. Therefore, the presence of amylin in the hetero-oligomer supports alpha-to-beta refolding on the raft surface. Furthermore, the presence of tau in the dimeric 1tam promotes the formation of beta-sheets of amylin, while no significant beta-sheet is evident in the amylin monomer alone in the 1am. Hence, the presence of tau in the 1tam facilitates the surface-induced alpha-to-beta transition in our raft membrane. The above surface-induced protein folding events of homo- and hetero-oligomers indicate that the hetero-oligomers have a similar propensity of expressing beta-sheets structures when compared with homo-tau or -amylin alone.

Note that this study focuses only on the 2D protein folding of pre-formed hetero-oligomers on the surface of a phase-separated raft membrane. In the absence of lipid membranes, 3D protein folding in a solution also occurs. Clearly, the energy landscapes of folding of oligomers in 3D solution may be more complex than those on a 2D surface. More future work on the protein folding of hetero-oligomers in a solution is still needed.

In summary, our comparative and analytical results on the binding patterns and membrane disruption of homo- and hetero-oligomers may serve as a mechanistic model of neural degeneration initiated by the binding of cross-seeded amylin and tau oligomers on the neuronal membrane. Note that the hetero-oligomerization of tau and amylin in solution and spectroscopic characterizations of amylin–tau hetero-oligomers have previously been reported in an *in vitro* study [7]. In addition, a recent *in vivo* study found that the amylin–tau hetero-oligomers indeed lead to neurotoxicity through neuroinflammation and neuronal dysfunction in mice [3]. Building upon these previous *in vitro* and *in vivo* research approaches, our findings allow for the identification of the specific amino acid residues of amylin (I16 and L26) and tau (N-terminal) responsible for protein binding to lipid rafts, as well as the global (domain size) and local (lipid order) membrane damage mechanisms leading to cytotoxicity. In addition, the *in vitro* study suggests an increase in beta-sheet formation, proceeding with amylin’s oligomerization [7]. Further substantiating this result, our findings on protein folding indicate that the amylin’s beta-sheet formation not only proceeds oligomerization, but is increased in the presence of tau, suggesting a synergistic interaction between tau and amylin in promoting the beta-sheet formation of amylin.

As indicated by a recent review [5], the clinical efficacy of current treatments of AZ are scarce, and the cross-talk between AZ and T2D is increasingly prevalent worldwide. Future preventive and therapeutic interventions for AZ require new knowledge of the protein–lipid interactions responsible for the membrane damage induced by the cross-seeded oligomers and the atomistic structures of the membrane-bound oligomers. Our mechanistic model and new atomistic membrane-bound oligomer structures may inspire future development of multipurpose drugs that can inhibit the initial protein–lipid interaction of cross-seeded oligomers with neurons and prevent the further aggregation of membrane-bound oligomers to form cytotoxic macromolecular structures that lead to neuronal death.

5. Conclusions

In conclusion, this computational study indicates that the hetero- and homo-oligomers prefer to bind to the Lod domain, and the membrane binding of either type of oligomer involves the L16 and I26 residues of the amylin and the *N*-terminal of the tau. The domain disruption effects caused by tetrameric 2tam were similar to those caused by the homo-oligomers of similar sizes. Dimeric 1tam has a much stronger local order disruption of DPPC than monomeric 1am, monomeric 1tau, or tetrameric 2tam. Finally, the presence of tau in the dimeric 1tam promotes the alpha-helix-to-beta-sheet transition of the constituent amylin when compared with the monomeric 1am alone. Our results will provide useful information for understanding the cross-seeding effects of amylin and tau on the membrane damage of neurons and for developing new therapeutic interventions targeting the formation of cytotoxic hetero-oligomers on neuronal membranes associated with Alzheimer's.

Supplementary Materials: The following supporting information can be downloaded at: <https://www.mdpi.com/article/10.3390/macromol3040046/s1>, Figure S1: Modeling of homogeneous oligomers, Figure S2: Minimum distance analysis of 1tam binding to the raft membrane, Figure S3: Minimum distance analysis of 2tam binding to the raft membrane, Figure S4: Mindist heatmaps of 1tam/raft complexes, Figure S5: Mindist heatmaps of 2tam/raft complexes, Figure S6: Compositions of annular lipids of membrane-bound oligomers, Figure S7: Phospholipid order disruptions by hetero- and homo-amylin-oligomers, Figure S8: Protein structures of membrane-bound homo-amylin and -tau oligomers; Figure S9: Contact maps of membrane-bound hetero-oligomers. Video S1: Self-aggregation of 1tam in solution, Video S2: Self-aggregation of 2tam in solution, Video S3: Binding of 1tam to raft membrane in lateral view, Video S4: Binding of 1tam to raft membrane in transverse view. All the videos can be found in <https://data.mendeley.com/datasets/8vb23c48ph/1> (accessed on 13 October 2023).

Author Contributions: Conceptualization, A.L. and K.H.C.; methodology, T.P. and K.H.C.; software, N.S., L.S., A.L., T.P. and K.H.C.; validation, N.S., L.S. and K.H.C.; formal analysis, N.S., L.S. and K.H.C.; investigation, N.S., L.S., A.L., T.P. and K.H.C.; resources, K.H.C.; data curation, K.H.C.; writing—original draft preparation, N.S., L.S. and K.H.C.; writing—review and editing, N.S. and K.H.C.; visualization, L.S. and K.H.C.; supervision, K.H.C.; project administration, K.H.C.; funding acquisition, K.H.C. All authors have read and agreed to the published version of the manuscript.

Funding: This research was funded by the Robert A. Welch Foundation Grant W-2057-20210327, National Science Foundation (OAC 1531594), National Institutes of Health (RC1-GM090897), and Williams Endowment of Interdisciplinary Physics of Trinity University.

Institutional Review Board Statement: Not applicable.

Informed Consent Statement: Not applicable.

Data Availability Statement: Data are contained within the article and Supplementary Materials.

Acknowledgments: We thank Neal Pape of Trinity University for his help in installing and maintaining the NSF-funded High-Performance Computer cluster, which was crucial to the MD simulation work. We also thank M. Blumer and M. C. Owen for providing instructions for setting up the lipid force fields of DLPC.

Conflicts of Interest: The authors declare no conflict of interest.

Abbreviations

AA	all-atom
CG	coarse-grained
MD	molecular dynamics
1am	monomeric amylin
2am	dimeric amylin oligomer
4am	tetrameric amylin oligomer
1tau	monomeric tau
2tau	dimeric tau oligomer

4tau	tetrameric tau oligomer
1tam	dimeric tau-amylin oligomer
2tam	tetrameric tau-amylin oligomer
PC	phosphatidylcholine
CHOL	cholesterol
DPPC	dipalmitoyl-PC
DLPC	dilinoleoyl-PC
Lo	liquid-ordered
Ld	liquid-disordered
Lod	mixed Lo/Ld
AL	annular lipid
nAL	non-annular lipid
<i>mindist</i>	minimum distance
DSSP	Define Secondary Structure of Proteins

References

- Milardi, D.; Gazit, E.; Radford, S.E.; Xu, Y.; Gallardo, R.U.; Cafilisch, A.; Westermark, G.T.; Westermark, P.; Rosa, C.; Ramamoorthy, A. Proteostasis of Islet Amyloid Polypeptide: A Molecular Perspective of Risk Factors and Protective Strategies for Type II Diabetes. *Chem. Rev.* **2021**, *121*, 1845–1893. [[CrossRef](#)]
- Gerson, J.E.; Castillo-Carranza, D.L.; Kaye, R. Advances in therapeutics for neurodegenerative tauopathies: Moving toward the specific targeting of the most toxic tau species. *ACS Chem. Neurosci.* **2014**, *5*, 752–769. [[CrossRef](#)]
- Zhang, G.; Meng, L.; Wang, Z.; Peng, Q.; Chen, G.; Xiong, J.; Zhang, Z. Islet amyloid polypeptide cross-seeds tau and drives the neurofibrillary pathology in Alzheimer's disease. *Mol. Neurodegener.* **2022**, *17*, 12. [[CrossRef](#)] [[PubMed](#)]
- Zhu, H.; Tao, Q.; Ang, T.F.A.; Massaro, J.; Gan, Q.; Salim, S.; Zhu, R.Y.; Kolachalama, V.B.; Zhang, X.; Devine, S.; et al. Association of Plasma Amylin Concentration With Alzheimer Disease and Brain Structure in Older Adults. *JAMA Netw. Open* **2019**, *2*, e199826. [[CrossRef](#)] [[PubMed](#)]
- Bortoletto, A.S.; Parchem, R.J. A pancreatic player in dementia: Pathological role for islet amyloid polypeptide accumulation in the brain. *Neural Regen. Res.* **2023**, *18*, 2141–2146. [[PubMed](#)]
- Wijesekara, N.; Goncalves, R.A.; Ahrens, R.; Ha, K.; De Felice, F.G.; Fraser, P.E. Combination of human tau and islet amyloid polypeptide exacerbates metabolic dysfunction in transgenic mice. *J. Pathol.* **2021**, *254*, 244–253. [[CrossRef](#)] [[PubMed](#)]
- Arya, S.; Claud, S.L.; Cantrell, K.L.; Bowers, M.T. Catalytic Prion-Like Cross-Talk between a Key Alzheimer's Disease Tau-Fragment R3 and the Type 2 Diabetes Peptide IAPP. *ACS Chem. Neurosci.* **2019**, *10*, 4757–4765. [[CrossRef](#)] [[PubMed](#)]
- Akter, R.; Cao, P.; Noor, H.; Ridgway, Z.; Tu, L.H.; Wang, H.; Wong, A.G.; Zhang, X.; Abedini, A.; Schmidt, A.M.; et al. Islet Amyloid Polypeptide: Structure, Function, and Pathophysiology. *J. Diabetes Res.* **2016**, *2016*, 2798269. [[CrossRef](#)] [[PubMed](#)]
- Bharadwaj, P.; Solomon, T.; Sahoo, B.R.; Ignasiak, K.; Gaskin, S.; Rowles, J.; Verdile, G.; Howard, M.J.; Bond, C.S.; Ramamoorthy, A.; et al. Amylin and beta amyloid proteins interact to form amorphous heterocomplexes with enhanced toxicity in neuronal cells. *Sci. Rep.* **2020**, *10*, 10356. [[CrossRef](#)]
- Sciacca, M.F.M.; La Rosa, C.; Milardi, D. Amyloid-Mediated Mechanisms of Membrane Disruption. *Biophysica* **2021**, *1*, 137–156. [[CrossRef](#)]
- Shafiee, S.S.; Guerrero-Munoz, M.J.; Castillo-Carranza, D.L. Tau Oligomers: Cytotoxicity, Propagation, and Mitochondrial Damage. *Front. Aging Neurosci.* **2017**, *9*, 83. [[CrossRef](#)]
- Cao, Q.; Boyer, D.R.; Sawaya, M.R.; Ge, P.; Eisenberg, D.S. Cryo-EM structure and inhibitor design of human IAPP (amylin) fibrils. *Nat. Struct. Mol. Biol.* **2020**, *27*, 653–659. [[CrossRef](#)]
- Fitzpatrick, A.W.P.; Falcon, B.; He, S.; Murzin, A.G.; Murshudov, G.; Garringer, H.J.; Crowther, R.A.; Ghetti, B.; Goedert, M.; Scheres, S.H.W. Cryo-EM structures of tau filaments from Alzheimer's disease. *Nature* **2017**, *547*, 185–190. [[CrossRef](#)]
- Cheng, K.H.; Graf, A.; Lewis, A.; Pham, T.; Acharya, A. Exploring Membrane Binding Targets of Disordered Human Tau Aggregates on Lipid Rafts Using Multiscale Molecular Dynamics Simulations. *Membranes* **2022**, *12*, 1098. [[CrossRef](#)]
- Lewis, A.; Pham, T.; Nguyen, N.; Graf, A.; Cheng, K.H. Lipid domain boundary triggers membrane damage and protein folding of human islet amyloid polypeptide in the early pathogenesis of amyloid diseases. *Biophys. Chem.* **2023**, *296*, 106993. [[CrossRef](#)] [[PubMed](#)]
- Wassenaar, T.A.; Pluhackova, K.; Bockmann, R.A.; Marrink, S.J.; Tieleman, D.P. Going Backward: A Flexible Geometric Approach to Reverse Transformation from Coarse Grained to Atomistic Models. *J. Chem. Theory Comput.* **2014**, *10*, 676–690. [[CrossRef](#)] [[PubMed](#)]
- Sali, A.; Blundell, T.L. Comparative protein modelling by satisfaction of spatial restraints. *J. Mol. Biol.* **1993**, *234*, 779–815. [[CrossRef](#)] [[PubMed](#)]
- Monticelli, L.; Kandasamy, S.K.; Periole, X.; Larson, R.G.; Tieleman, D.P.; Marrink, S.J. The MARTINI Coarse-Grained Force Field: Extension to Proteins. *J. Chem. Theory Comput.* **2008**, *4*, 819–834. [[CrossRef](#)]
- Hess, B.; Kutzner, C.; van der Spoel, D.; Lindahl, E. GROMACS 4: Algorithms for Highly Efficient, Load-Balanced, and Scalable Molecular Simulation. *J. Chem. Theory Comput.* **2008**, *4*, 435–447. [[CrossRef](#)] [[PubMed](#)]

20. Han, B.; Tashjian, A.H. User-friendly and versatile software for analysis of protein hydrophobicity. *BioTechniques* **1998**, *25*, 256–263. [[CrossRef](#)] [[PubMed](#)]
21. Kyte, J.; Doolittle, R.F. A simple method for displaying the hydropathic character of a protein. *J. Mol. Biol.* **1982**, *157*, 105–132. [[CrossRef](#)]
22. Cebeacauer, M.; Amaro, M.; Jurkiewicz, P.; Sarmiento, M.J.; Sachl, R.; Cwiklik, L.; Hof, M. Membrane Lipid Nanodomains. *Chem. Rev.* **2018**, *118*, 11259–11297. [[CrossRef](#)]
23. De Wit, G.; Danial, J.S.; Kukura, P.; Wallace, M.I. Dynamic label-free imaging of lipid nanodomains. *Proc. Natl. Acad. Sci. USA* **2015**, *112*, 12299–12303. [[CrossRef](#)]
24. Sezgin, E.; Levental, I.; Mayor, S.; Eggeling, C. The mystery of membrane organization: Composition, regulation and roles of lipid rafts. *Nat. Rev. Mol. Cell Biol.* **2017**, *18*, 361–374. [[CrossRef](#)]
25. Simons, K.; Sampaio, J.L. Membrane organization and lipid rafts. *Cold Spring Harb. Perspect. Biol.* **2011**, *3*, a004697. [[CrossRef](#)]
26. Pham, T.; Cheng, K.H. Exploring the binding kinetics and behaviors of self-aggregated beta-amyloid oligomers to phase-separated lipid rafts with or without ganglioside-clusters. *Biophys. Chem.* **2022**, *290*, 106874. [[CrossRef](#)]
27. Risselada, H.J.; Marrink, S.J. The molecular face of lipid rafts in model membranes. *Proc. Natl. Acad. Sci. USA* **2008**, *105*, 17367–17372. [[CrossRef](#)]
28. Humphrey, W.; Dalke, A.; Schulten, K. VMD: Visual molecular dynamics. *J. Mol. Graph.* **1996**, *14*, 33–38. [[CrossRef](#)]
29. Maier, J.A.; Martinez, C.; Kasavajhala, K.; Wickstrom, L.; Hauser, K.E.; Simmerling, C. ff14SB: Improving the Accuracy of Protein Side Chain and Backbone Parameters from ff99SB. *J. Chem. Theory Comput.* **2015**, *11*, 3696–3713. [[CrossRef](#)]
30. Blumer, M.; Harris, S.; Li, M.; Martinez, L.; Untereiner, M.; Saeta, P.N.; Carpenter, T.S.; Ingolfsso, H.I.; Bennett, W.F.D. Simulations of Asymmetric Membranes Illustrate Cooperative Leaflet Coupling and Lipid Adaptability. *Front. Cell Dev. Biol.* **2020**, *8*, 575. [[CrossRef](#)]
31. Grote, F.; Lyubartsev, A.P. Optimization of Slipids Force Field Parameters Describing Headgroups of Phospholipids. *J. Phys. Chem. B* **2020**, *124*, 8784–8793. [[CrossRef](#)]
32. Kabsch, W.; Sander, C. Dictionary of protein secondary structure: Pattern recognition of hydrogen-bonded and geometrical features. *Biopolymers* **1983**, *22*, 2577–2637. [[CrossRef](#)]
33. Mercadante, D.; Grater, F.; Daday, C. CONAN: A Tool to Decode Dynamical Information from Molecular Interaction Maps. *Biophys. J.* **2018**, *114*, 1267–1273. [[CrossRef](#)]
34. Brender, J.R.; McHenry, A.J.; Ramamoorthy, A. Does cholesterol play a role in the bacterial selectivity of antimicrobial peptides? *Front. Immunol.* **2012**, *3*, 195. [[CrossRef](#)]
35. Hasan, M.; Moghal, M.M.R.; Saha, S.K.; Yamazaki, M. The role of membrane tension in the action of antimicrobial peptides and cell-penetrating peptides in biomembranes. *Biophys. Rev.* **2019**, *11*, 431–448. [[CrossRef](#)]
36. Yang, S.T.; Kiessling, V.; Tamm, L.K. Line tension at lipid phase boundaries as driving force for HIV fusion peptide-mediated fusion. *Nat. Commun.* **2016**, *7*, 11401. [[CrossRef](#)]
37. Akimov, S.A.; Kuzmin, P.I.; Zimmerberg, J.; Cohen, F.S. Lateral tension increases the line tension between two domains in a lipid bilayer membrane. *Phys. Rev. E Stat. Nonlin Soft Matter Phys.* **2007**, *75 Pt 1*, 011919. [[CrossRef](#)]
38. Belicka, M.; Weitzer, A.; Pabst, G. High-resolution structure of coexisting nanoscopic and microscopic lipid domains. *Soft Matter* **2017**, *13*, 1823–1833. [[CrossRef](#)]
39. Pinigin, K.V.; Kondrashov, O.V.; Jimenez-Munguia, I.; Alexandrova, V.V.; Batishchev, O.V.; Galimzyanov, T.R.; Akimov, S.A. Elastic deformations mediate interaction of the raft boundary with membrane inclusions leading to their effective lateral sorting. *Sci. Rep.* **2020**, *10*, 4087. [[CrossRef](#)]
40. Nanga, R.P.; Brender, J.R.; Vivekanandan, S.; Ramamoorthy, A. Structure and membrane orientation of IAPP in its natively amidated form at physiological pH in a membrane environment. *Biochim. Biophys. Acta* **2011**, *1808*, 2337–2342. [[CrossRef](#)]
41. Khemtouri, L.; Fatafta, H.; Davion, B.; Lecomte, S.; Castano, S.; Strodel, B. Structural Dissection of the First Events Following Membrane Binding of the Islet Amyloid Polypeptide. *Front. Mol. Biosci.* **2022**, *9*, 849979. [[CrossRef](#)]
42. Brender, J.R.; Hartman, K.; Reid, K.R.; Kennedy, R.T.; Ramamoorthy, A. A single mutation in the nonamyloidogenic region of islet amyloid polypeptide greatly reduces toxicity. *Biochemistry* **2008**, *47*, 12680–12688. [[CrossRef](#)]
43. Engel, M.F.; Khemtouri, L.; Kleijer, C.C.; Meeldijk, H.J.; Jacobs, J.; Verkleij, A.J.; de Kruijff, B.; Killian, J.A.; Hoppener, J.W. Membrane damage by human islet amyloid polypeptide through fibril growth at the membrane. *Proc. Natl. Acad. Sci. USA* **2008**, *105*, 6033–6038. [[CrossRef](#)]
44. Sepehri, A.; Nepal, B.; Lazaridis, T. Distinct Modes of Action of IAPP Oligomers on Membranes. *J. Chem. Inf. Model.* **2021**, *61*, 4645–4655. [[CrossRef](#)]
45. Sulatskaya, A.I.; Kosolapova, A.O.; Bobylev, A.G.; Belousov, M.V.; Antonets, K.S.; Sulatsky, M.I.; Kuznetsova, I.M.; Turoverov, K.K.; Stepanenko, O.V.; Nizhnikov, A.A. β -Barrels and Amyloids: Structural Transitions, Biological Functions, and Pathogenesis. *Int. J. Mol. Sci.* **2021**, *22*, 11316. [[CrossRef](#)]

Disclaimer/Publisher’s Note: The statements, opinions and data contained in all publications are solely those of the individual author(s) and contributor(s) and not of MDPI and/or the editor(s). MDPI and/or the editor(s) disclaim responsibility for any injury to people or property resulting from any ideas, methods, instructions or products referred to in the content.